UNIVERSITY OF CALIFORNIA,
IRVINE

Characterization of Microscopic Thermofluidic Transport for Development of Porous Media Used in Phase-Change Devices

DISSERTATION

Submitted in partial satisfaction of the requirements
for the degree of

MASTER OF SCIENCE
in Mechanical and Aerospace Engineering

by

Youngjoon Suh

Dissertation Committee:
Assistant Professor Yoonjin Won, Chair
Professor Yun Wang
Assistant Professor Iryna Zenyuk

DEDICATION

To my loving wife Hyunju and daughter Eliana whose unyielding love, support, and encouragement have enriched my soul and inspired me to continue this research.

TABLE OF CONTENTS

LIST OF FIGURES

ACKNOWLEDGEMENTS

Primarily I would like to thank God without whom nothing is possible.

I am grateful to my advisor, Yoonjin Won, for supporting my projects and giving me the opportunity to conduct research in her group.

I would also like to acknowledge my family in Korea for their encouragement and prayers along the way.

Thank you Hyunju, for your unwavering belief in me.

Finally, thank you Eliana, for training me to work unlimited nights deprived of sleep.

CURRICULUM VITAE

Youngjoon Suh

EDUCATION

Master of Science in Mechanical Engineering 2020

University of California, Irvine *Irvine, California*

Bachelor of Science in Mechanical Engineering 2016

Chung-Ang University, Seoul, Korea

Dongjak-gu, Seoul

RESEARCH EXPERIENCE

Graduate Research Assistant 2017-2020

University of California, Irvine *Irvine, California*

Research Assistant 2016-2017

Chung-Ang University, Seoul, Korea

Dongjak-gu, Seoul

TEACHING EXPERIENCE

Teaching Assistant 2017-2020

University of California, Irvine *Irvine, California*

JOURNAL PUBLICATIONS

Evaporation Rate Measurement at Multiple Scales Using Temperature-Sensitive Fluorescence Dyes 2020

Y. Suh, C.H. Lin, H. Gowda, and Y. Won, *Journal of Electronic Packaging*, *Accepted*

***in situ* Experimental Evidence for Interparticle Interactions in Colloidal Assemblies Using Micro Laser Induced Fluorescence Microscopy** 2020

Y. Suh, H. Gowda, and Y. Won, *Submitted*

The Control of Colloidal Grain Boundaries through Evaporative Vertical Self-Assembly 2019

Y. Suh, Q. Pham, B. Shao, and Y. Won, *Small*, 15 (12), 1804523

Capillary Wicking in Hierarchically Textured Copper Nanowire Arrays 2018

J. Lee, Y. Suh, P.P. Dubey, M. T. Barako, and Y. Won,

ACS Applied Materials & Interfaces, 11 (1), 1546-1554

Effect of Off-Plane Bifurcation Angles of Primary Bronchi on Expiratory Flows in the Human Trachea 2018

Y. Suh, J.Y. Park, *Computers in Biology and Medicine*, 95, 63-74

A Paired Bead and Magnet Array for Molding Microwells with Variable Concave Geometries 2018

G.H. Lee, Y. Suh, and J.Y. Park, *Journal of Visualized Experiments*, e55548

CONFERENCE PRESENTATIONS

Evaporation Rate Measurement at Multiple Scales Using Temperature-Sensitive Fluorescence Dyes Oct. 2019

International Technical Conference and Exhibition of Packaging and Integration of Electronic and Photonic Microsystems (InterPACK), Anaheim, CA, USA

Boiling Heat Transfer Using Spatially-Variant and Uniform Microporous Coatings Oct. 2019

ASME 2019 International Technical Conference and Exhibition of Packaging and Integration of Electronic and Photonic Microsystems (InterPACK), Anaheim, CA, USA

Microstructural Patterning of Self-Assembled Colloidal Particles Jun. 2019

17th International Conference on Nanochannels, Microchannels, and Minichannels (ICNMM), St. John's, Newfoundland, Canada

HONORS AND AWARDS

Best Poster Award, 17th International Conference on Nanochannels, Microchannels, and Minichannels (2019)

Cum Laude Graduation, Chung-Ang University (2016)

Merit-based Scholarship, Chung-Ang University (2011-2015)

Scholarship, National Agricultural Cooperative Federation (2014)

ABSTRACT OF THE DISSERTATION

Characterization of Microscopic Thermofluidic Transport for Development of Porous Media Used in Phase-Change Devices

By

Youngjoon Suh

Master of Science in Mechanical and Aerospace Engineering

University of California, Irvine, 2020

Assistant Professor Yoonjin Won, Chair

As the heat generation at the device footprint continuously increases in modern high-tech electronics, there is an urgent need to develop cooling devices that can dissipate highly concentrated heat loads. Phase-change cooling strategies leverage the high latent heat of vaporization of the working fluid to effectively dissipate large heat fluxes. Typical passive two-phase cooling devices utilize the thermal and fluidic transport properties of porous microstructures called the wick that facilitate evaporative heat transfer. Despite the increasing attention that the wick receives for phase-change devices, developing the optimal wick has been a daunting challenge due to the limited resolution of extant thermofluidic characterization techniques. From the designing perspective, it has been difficult to precisely predict how microstructures affect thermofluidic transport through traditional low-resolution experiments. From the manufacturing perspective, large-scale (> 100 μm) fabrication of self-assembled wick templates are restricted due to solvent evaporation-induced structural defects called grain boundaries. Motivated by this multistep task, this thesis reports experimental characterization of multiscale thermal and fluidic

transport phenomena occurring in porous media using a novel micro laser induced fluorescence (μLIF) technique.

Primarily, we corroborate the use of unsealed temperature-sensitive dyes by systematically investigating their effects on temperature, concentration, and liquid thickness on the fluorescence intensity. Considering these factors, we analyze the evaporative performances of microstructures using two approaches. The first approach characterizes local and overall evaporation rates by measuring the solution drying time. The second method employs an intensity-to-temperature calibration curve to convert temperature-sensitive fluorescence signals to surface temperatures. Then, submicron-level evaporation rates are calculated by employing a species transport equation for vapor at the liquid-vapor interface. Using these methods, we decompose key thermofluidic parameters contributing to the wick's evaporative performance.

We then extend this work to study *in situ* interparticle interactions in colloidal assemblies that decide grain boundaries in colloidal wick templates. The fluorescence microscopy measures the saturation levels with high fidelity to identify distinct colloidal structuring regimes during self-assembly as well as cracking mechanics.

The presented studies help decompose the key thermofluidic parameters contributing to the evaporative performance of microscale structures and offer fundamental groundworks for developing large-scale crack-free colloidal wick templates using colloidal self-assembly fabrication.

Chapter 1
Introduction

1.1. Thermal Management

Thermal management has become a bottleneck for a variety of modern high-tech devices such as integrated circuits, solar energy converters, laser diodes, and microprocessors where heat generation at the device footprint has long surpassed 100 W/cm^2 (Figure 1.1).[1-3] At small scales, the local hot-spots in today's chip designs are starting to report massive heat fluxes up to 300 W/cm^2.[4, 5] Such extreme heat loads reduce device performance, reliability, and lifetime. Consequently, thermal engineers search for efficient thermal management strategies.

An attractive cooling strategy that has superior heat removal capacities compared to traditional conductive solid-state heat spreaders or forced air convection is phase-change heat transfer.[6] In

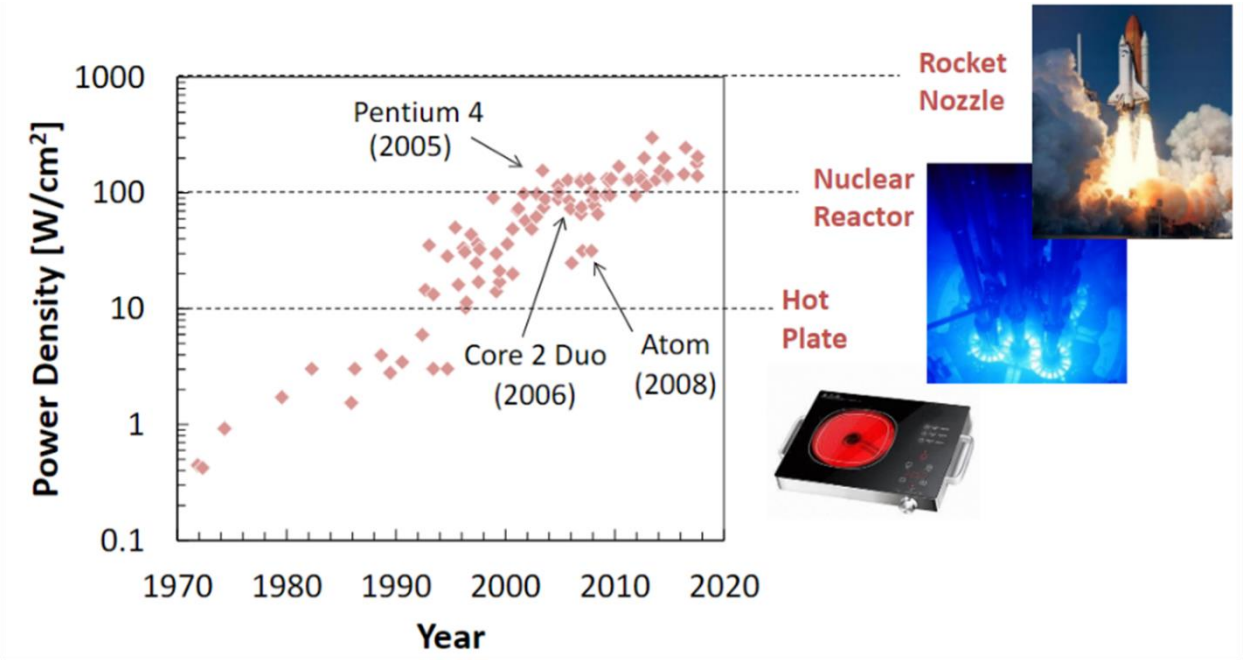

Figure 1.1: Microprocessor evolution and thermal management challenges.[1]

particular, liquid-to-vapor phase change solutions utilize the working fluid's high energy absorption during phase change (i.e., latent heat) to dissipate a great amount of heat within a small difference of temperature. Existing phase-change-based cooling strategies include pool boiling,[7] flow boiling,[8] jet impingement,[9] spray cooling,[10] and thin-film evaporation.[11, 12] Among various strategies to improve two-phase heat transfer performances, methods utilizing thermofluidic transport properties of porous media have especially garnered increasing attention owing to the advance in micro/nanofabrication techniques.

1.2. Utilization of Porous Media in Phase-Change Devices

Two-phase cooling devices, such as vapor chambers,[13] capillary pumped loop heat pipes,[13, 14] loop heat pipes,[13-16] and thermosyphon heat pipes,[17] operate in an evaporation, liquid-transport, and condensation cycle that utilize micro/nanoscale porous media called the wick (Figure 1.2).[13] The wick plays a vital role within the cooling devices by vaporizing, absorbing, and transporting the working fluid to maximize heat dissipation. Therefore, an optimal wick should have properties such as efficient working-fluid delivery (i.e., permeability),[15, 18] large surface area to volume ratios,[19] low thermal resistance,[17] and high effective thermal conductivity.[17]

1.3. Microscopic Thermofluidic Characterization

Building the optimal wick is a two-step challenge which can be aided by microscopic thermofluidic characterization. The first step is characterizing the real-time, high-resolution thermofluidic transport occurring in local parts of the wick. Many experimental heat transfer literatures analyze the wick's heat transfer performance at the device scale,[15, 20-22] which makes designing optimal wicks an arduous, trial-and-error task. On the other hand, microscale thermofluidic

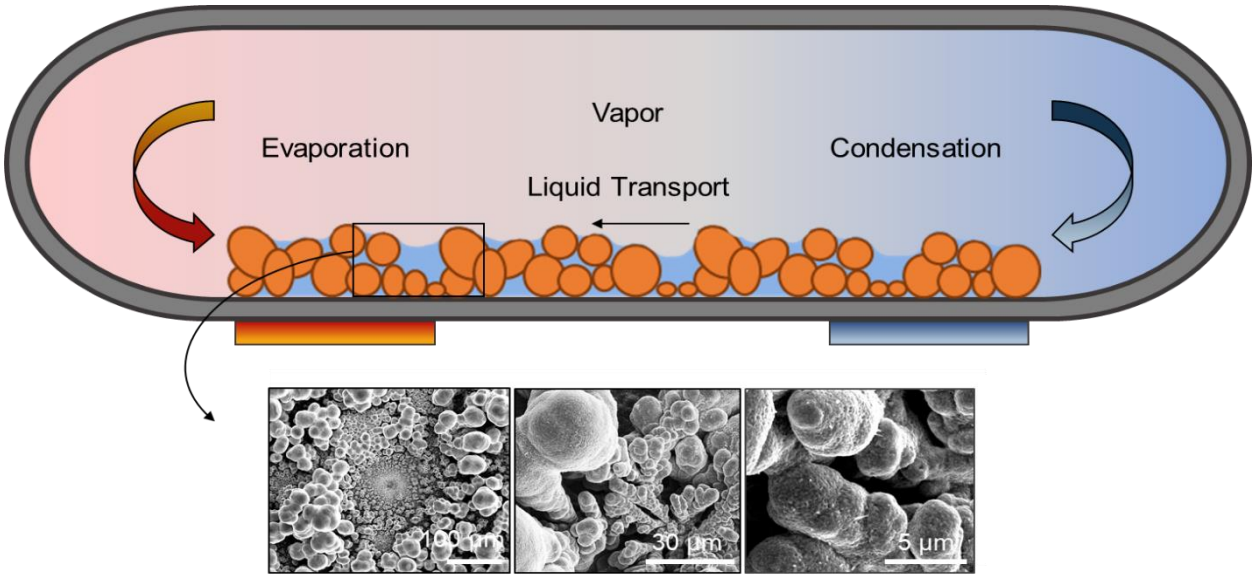

Figure 1.2: A schematic of a heat pipe. The working fluid is vaporized via thin film evaporation in the heated area and is transported towards the heat sink where the vapor condenses. After condensation, the working fluid is transported back towards the heated area via capillary-assisted liquid delivery through microporous media.

characterization can be used to decompose interplaying thermophysical parameters such as permeability, thermal conductivity, and effective surface areas to accurately predict and optimize the wick's evaporative performance. The next step is realizing wick designs through precise thermofluidic characterization. The recent advances in micro/nanofabrication has facilitated the designing of novel wick architectures that have enhanced liquid transport properties and higher surface area to volume ratios than traditional porous media such as channels, meshes, and sintered particles.[23, 24] However, several solvent-based micro/nanofabrication techniques such as colloidal self-assembly are subject to evaporation-induced microscale defects called grain boundaries, or microcracks, that limit large-scale production.[25] In order to eliminate or control these undesirable structural irregularities, high-resolution thermofluidic characterization of

interparticle interactions are required to fully interpret governing mechanisms that lead to the grain boundaries.

Over the past several decades, numerous methods have emerged to improve spatial and thermal resolution. For example, infrared (IR) thermography measures two-dimensional temperature profiles based on sample thermal emission.[26-30] However, IR imaging is limited to the scales above 3 – 5 μm due to the wavelength diffraction limit measured in the camera (> 3 μm).[29, 31] Another popular method is thermochromic liquid crystal thermography (TLC), which uses temperature-sensitive colors reflected by crystals to measure temperatures with up to 0.1 K thermal resolution.[29, 32-35] While TLC measurements support high resolution, the samples need additional treatment such as thin and uniform coatings to increase spatial resolution,[29, 35] which makes it unsuitable for observing unpaintable objects such as porous material.[29] Direct measurement employing scanning thermal microscopy (SThM) uses nanoscale probe apexes to map thermal profiles at high-resolutions (~30 nm).[36-38] However, the contact area of the probe to the sample can vary depending on the local sample geometry, which can lead to contact-related artifacts.[39, 40] Finally, micro-thermocouple probes prove the most conventional among the measuring techniques; they are cheap and accurate, but too large to probe into submicron-level features without damaging the structure (i.e., smallest micro-thermocouple commercially available is 13-50 μm).[35]

1.4. Micro Laser Induced Fluorescence Microscopy

As an emerging technique, laser induced fluorescence (LIF) gains attention as a powerful tool to characterize thermal profiles at multiple scales with high fidelity. In general, LIF utilizes

temperature-and light-sensitive molecules called fluorophores. At the macroscale, LIF has been conventionally used to analyze bulk thermofluidic physics typically over the mm scale.[41-43] On the other hand, micro laser induced fluorescence (μLIF) employs fluorescent microscopes to improve spatial and thermal resolutions up to 0.1 – 0.3 μm and 0.01 K, respectively. [31, 44-51] The methods generally employ fluorescence, where temperature-sensitive fluorophores absorb photons of a specific wavelength (i.e., excitation) and emit photons of a longer wavelength (i.e., emission) (Figure 1.3). The emitted fluorescence signals are selectively transmitted through an

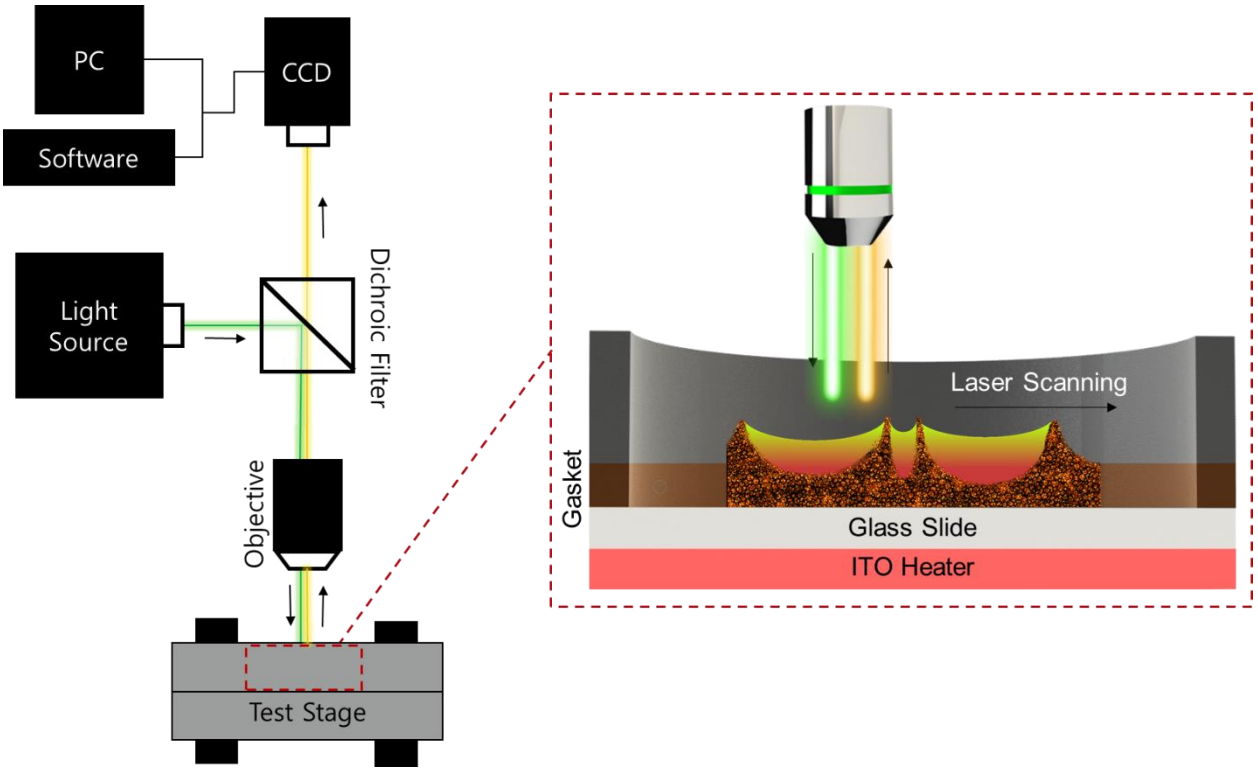

Figure 1.3: Diagram of micro laser induced fluorescence (μLIF). In μLIF measurements, a light source (green) excites the fluorophores, causing it to emit light at a higher wavelength. The light passes through an optical filter to a charge-coupled device (CCD) camera and is postprocessed in PC with software. The inset shows a typical test stage used in experiments for solutions entrapped in porous media.

optical filter to produce fluorescence intensity-based imaging, which is then converted into temperature-based pictures. A great advantage of using μLIF is to observe temporal micro/nanoscale pixel-based fluorescent intensity profiles of the liquid-vapor interface. In other words, even some of the smallest liquid-vapor surface features are easily detected by observing fluorescence signals and can be used to assess local drying phenomena in complex structures.

Although μLIF techniques have shown potential to function as thermometers in closed systems,[31, 45, 48] there have been no efforts to identify microscopic thermofluidic transport in open (where solvent is evaporating) or colloidal (where non-temperature-sensitive nanoparticles are added) systems. In an evaporating system, thin-film solvent evaporation effects on fluorescence behavior are complicated because the liquid film thickness and dye concentration simultaneously change upon evaporation. In colloidal systems, the fluorescence behavior becomes even more complex due to the influence of doped nanoparticles.

1.5. Scope of the Thesis

The objective of this thesis is to experimentally investigate real-time submicron scale thermofluidic phenomena using μLIF techniques with the aim to optimize wick design and fabrication.

In Chapter 2, we systematically present methods to characterize evaporative phenomena in an open system by using μLIF techniques at both large (~1 cm) and local (0.3 – 35 μm) scales. We utilize fluorescence signals emitted from evaporating solutions in porous microstructures to decompose interplaying thermofluidic parameters that influence the wick's evaporative performance.

In Chapter 3, we use the same μLIF system mentioned in Chapter 2 to experimentally characterize real-time colloid physics during self-assembly at the submicron scale. High-resolution

measurements allow us to examine the detailed interparticle interactions during evaporative self-assembly, resulting in the formation of grain boundaries or microcracks between crystal opals and their propagation.

In Chapter 4, summarizes the key findings of this thesis and outline future work.

Chapter 2

Multiscale Evaporation Rate Measurement

2.1. Introduction

As modern electronics continuously exceed their performance limits, there is an urgent need to develop new cooling devices that balance the increasing power demands. To meet this need, cutting-edge cooling devices often utilize microscale structures that facilitate two-phase heat transfer. However, it has been difficult to understand how microstructures trigger enhanced evaporation performances through traditional experimental methods due to low spatial resolution. The previous methods can only provide coarse interpretations on how physical properties such as capillary pressure, permeability, and interfacial surface areas interact at the microscale to effectively dissipate heat.

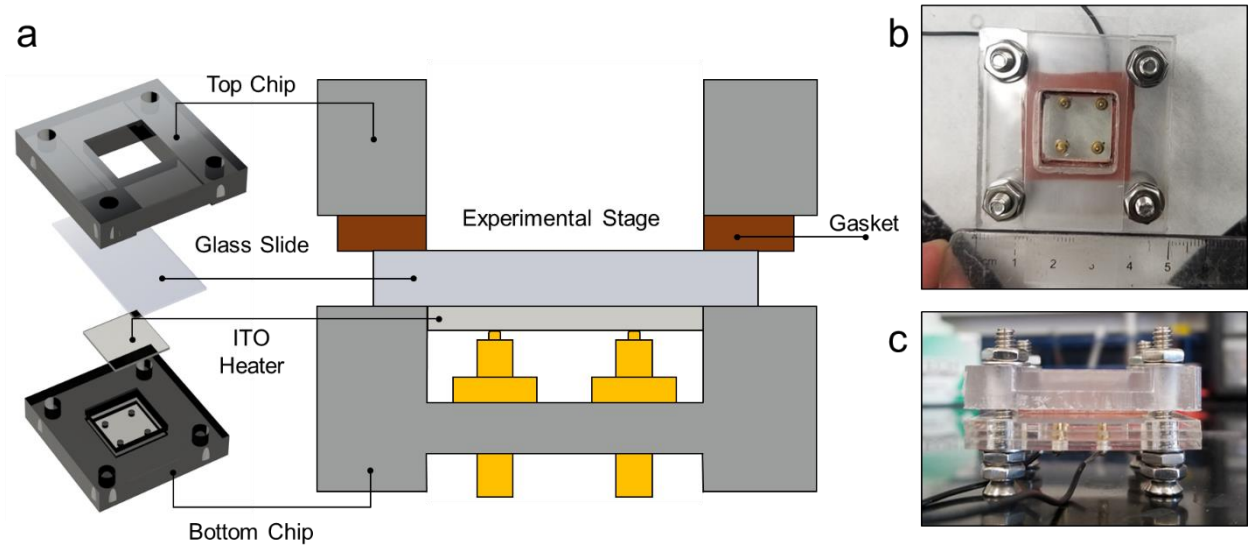

Figure 2.1: Experimental device setup. The chip consists of components shown in (a), which are easily assembled by fastening bolts and nuts. (b) Top and (c) cross-sectional views are shown.

In this Chapter, we experimentally characterize evaporative phenomena occurring within a biporous copper wick by using μLIF techniques at both large (~1 cm) and local (0.3 – 35 μm) scales. The experiments are conducted in an open system and considers the temperature, liquid thickness, and concentration effects on fluorescence intensity. For submicron level characterization, vapor transport equations are employed to calculate evaporation rates based on fluorescence intensity to temperature calibrations. Our results help decompose key physical parameters such as microscopic liquid flow paths that influence the wick's evaporative performance.

2.2. Test Device Design

A custom built evaporation chip is used for all experiments in this Chapter (Figure 2.1). The evaporation chip consists of top and bottom acrylic platforms, a removable glass slide, a rubber gasket, spring-loaded pogo pins, and a transparent indium-tin-oxide (ITO) heater. The top and bottom platforms are fabricated using a computer numerical control (CNC) router to provide rigid support for all components. The gasket is inserted between the glass slide and the top chip to prevent leakage by applying distributed pressure through bolts and nuts. A constant voltage is provided through a power supply to produce a constant heat flux of 0.75 Wcm^{-2} from the ITO heater to the glass slide.

2.3. Microfabrication

The wicks are fabricated using a simple template-assisted electrodeposition method. A 1 mm thick brass plate is cut into 1 cm × 3 cm sample pieces through machining processes. A copper sample used as the anode is prepared with identical dimensions. The brass and copper samples are immersed in hydrochloric acid for 15 minutes prior to electrodeposition. The electrodeposition

process is performed in a stationary 0.4 M CuSO4 + 1.8 M H2SO4 solution. A constant current density of 2 Acm^{-2} is applied for 3 minutes with a power supply.

2.4. Temperature-Sensitive Fluorescence Dye

We use laser grade rhodamine B (Acros Organics) to make a temperature-sensitive fluorescent working fluid. Prior to rhodamine B addition, a 0.1 M sodium carbonate-bicarbonate buffer at pH 9.4 is prepared to ensure proper dye color density. The buffer is made by adding 30 ml of 0.1 M sodium carbonate to 70 ml of 0.1 M sodium bicarbonate. The buffer is then diluted from 0.1 M to 0.2 mM, and rhodamine B is added to make a 2 mM solution. The rhodamine B solutions are filtered with a syringe filter (0.2 μm pore size) before the use.

2.5. Image Acquisition

To obtain real-time, fluorescence-based liquid-vapor interface images, we use both inverted and upright confocal fluorescence microscopes. The inverted microscope views objects from bottom to top and can greatly increase imaging precision by eliminating the need to continuously focus on dynamic liquid-vapor interfaces (Figure 2.2a). Accordingly, we use an inverted microscope (LSM 700, ZEISS) with a 10 mm long working distance objective to characterize the liquid thickness and concentration effects on fluorescence intensity. An appropriate filter set (559 nm excitation band pass and 570-800 nm emission band pass) with a broadband halogen illumination is used. On the other hand, the upright microscope enables surface imaging of opaque samples from top to bottom (Figure 2.2b). Hence, an upright microscope (BX61, Olympus) is used to characterize evaporative performances of opaque microscale structures. A minimal laser beam intensity of 0.3% (to reduce photobleaching) excites the fluid at wavelengths of 559 nm to fluoresce while a

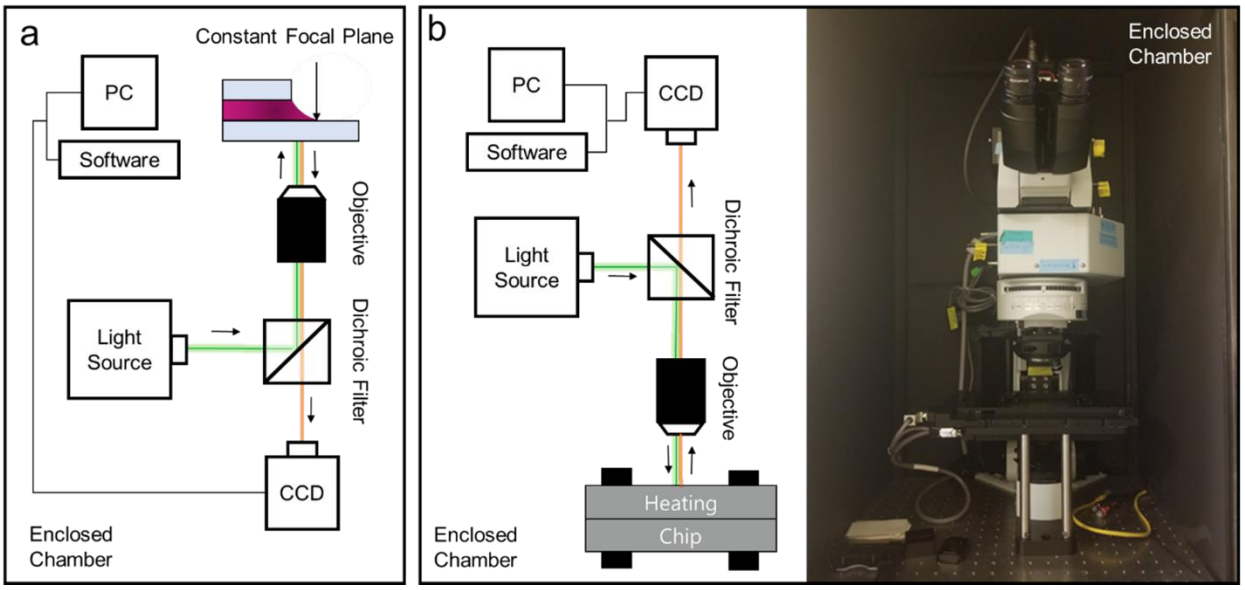

Figure 2.2: Inverted and upright microscope fluorescence imaging. (a) The inverted microscope views the sample from bottom to top while maintaining a constant focal plane. (b) On the other hand, the upright microscope views the surface of the liquid-vapor interfaces of the sample from the top to bottom view. (c) Experiments are conducted within an enclosed chamber environment to minimize external influences.

fluorimeter records the fluorescence spectra. The high voltage (HV) and gain are set manually and are kept constant throughout a given set of experiments. Digital images are obtained and post-processed with ZEN (ZEISS) and FluoView FV1000 (Olympus) software. Image colors are added through built-in channel options.

2.6. Rhodamine B Characterization

In this section, we corroborate the feasibility of using unsealed rhodamine B to characterize evaporative phenomena by systematically investigating the effects of temperature, liquid thickness, and concentration on fluorescence intensity.

2.6.1 Temperature Effect on Fluorescence Intensity

We investigate the dye's temperature-sensitivity by recording its fluorescence intensity and temperature profiles by using a heated microchip (Figure 2.3a). We minimize temperature variations within the microchip by using small dimensions (1 cm X 1 cm X 0.1 cm). Prior to imaging, the microchip is heated to ~75°C using a hotplate. Fluorescence images are captured every second as the microchip cools down while the solution temperature is recorded every 10 seconds with a pre-installed thermocouple. The fluorescence intensity increases as the solution temperature decreases as shown in Figure 2.3b. The fluorescence intensities are then normalized by the fluorescence intensity measured at room temperature (25°C), resulting in a calibration curve (Figure 2.3c), which is a fourth-order polynomial fit to the data of the form:

$$T = P_o + P_1 I + P_2 I^2 + P_3 I^3 + P_4 I^4 \quad (1)$$

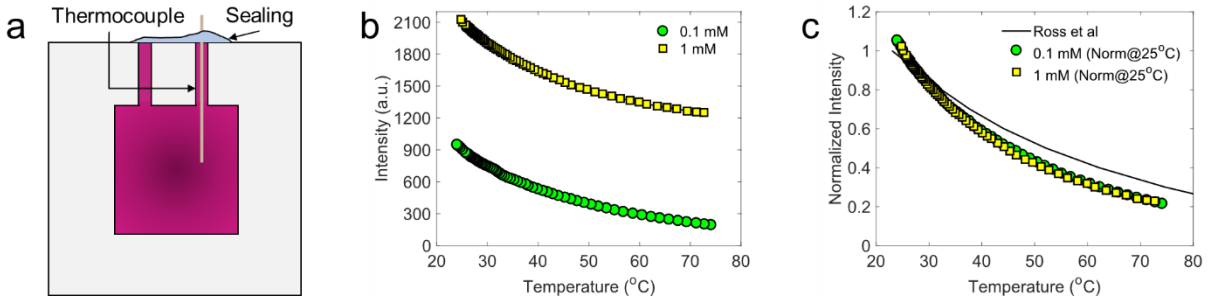

Figure 2.3: Temperature-dependent fluorescence intensity of rhodamine B (RhB). (a) Illustration of microchip. The chip has a preinstalled thermocouple and is sealed to prevent evaporation. (b) The plot shows the fluorescence intensity of RhB decreases as temperature increases. (c) The temperature-fluorescence intensity calibration curve is created by normalizing cold-field intensity values at 25°C.

where T is the temperature, I is the normalized fluorescence intensity, and P_o – P_4 are fitting constants: P_o = (128.7 ± 2.6)ºC, P_1 = (-359.5 ± 20.3)ºC, P_2 = (589.9 ± 54.8)ºC, P_3 = (-499.4 ± 61.5)ºC, and P_4 = (165 ± 24.5)ºC. The fitted line is relatively consistent even at different dye concentrations and matches very well with the past report of Ross et al. [48]

2.6.2 Liquid Thickness Effect on Fluorescence Intensity

To understand the liquid thickness effect on fluorescence intensity, we analyze a liquid meniscus trapped between two glass slides separated by 1 mm. The focal plane is fixed by focusing on a mark created at the bottom of the glass slide, as shown in Figure 2.4a. The meniscus is generated by pipetting 200 µl of rhodamine B solution between the glass slides. We discover an almost linear increase in fluorescence intensity until the liquid thickness reaches ~500 µm (Figure 2.4b). This is because the light passes through more solution at constant dye concentrations, thereby exciting more fluorophores. However, the fluorescence intensity reaches a plateau when the distance that light can penetrate through the solution is equal to the maximum distance that fluorescence can be sensed (Figure 2.4b). This relationship between liquid thickness and fluorescence intensity holds for different temperatures (Figure 2.4b). All the results above infer that varying liquid thickness has substantial influence on fluorescence intensity when the liquid thickness is < 500 µm but is less sensitive when liquid thicknesses is > 500 µm. Therefore, we minimize the effect of liquid thickness by maintaining a constant liquid thickness through a reservoir in later sections.

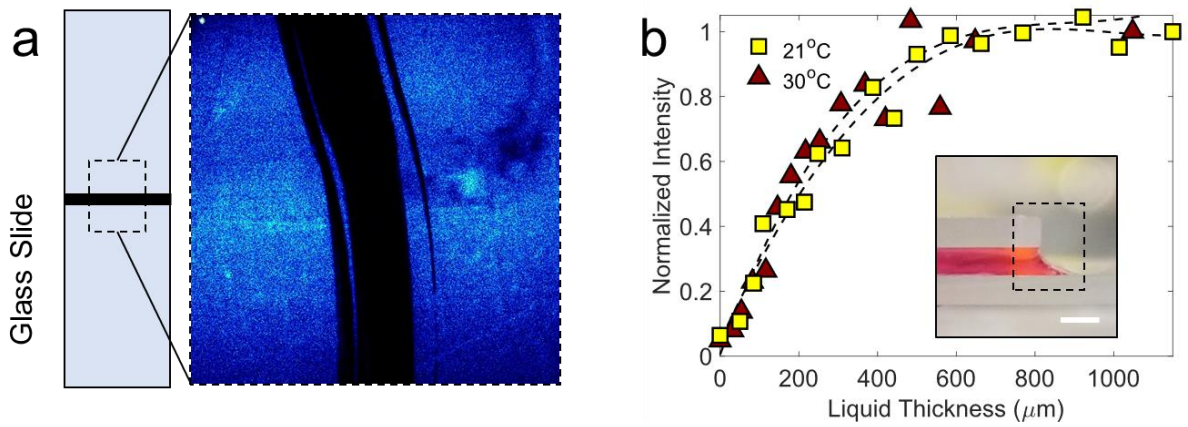

Figure 2.4: Medium thickness affects fluorescence intensity. (a) The focal length for inverted fluorescence microscopy is fixed by maintaining a constant focus on the bottom slide. The focal length is initially determined by focusing on a marker as shown. (b) The fluorescence intensity exhibits an almost linear increasing trend with liquid thickness up to ~ 500 μm. The measured fluorescence intensity values are normalized with intensity peak values for each experiment. Inset shows how a meniscus is formed between two glass slides. The scale bar is 1 mm.

2.6.3 Concentration Effect on Fluorescence Intensity

Finally, we quantify how dye concentration impacts fluorescence intensity in an open system environment. To do this, we compare two cases: In one case, we increase the dye concentration by evaporating the dye solution. In the second case, the dye concentration is kept constant while the liquid thickness is adjusted to match the former case. In detail, two 1 cm-diameter wells are filled with 1 mM rhodamine B solution, as shown in the inset of Figure 2.5a. The solution of one well is exposed to air at room temperature to promote evaporation, whereas the other is sealed to prevent it. The liquid thickness and fluorescence intensity are measured for both wells in sequential timesteps where the second well's solution is pulled out manually every timestep to match the first well's liquid thickness. Both well's fluorescence intensity increases as the solution evaporates

when the liquid thickness is below 1 mm which agrees with the previous section. The estimated evaporation-induced concentration variations with respect to liquid thickness from a known initial fluorophore mass is plotted in Figure 2.5a. The fluorescence intensity increases 30% as the concentration increases from 1 mM to 2 mM but reaches a relatively stable regime at concentrations 2 – 7 mM (Figure 2.5b). This trend is further validated through a separate case where concentration is increased by adding fluorophores at a fixed volume (Figure 2.5b). The 15% – 20% error between the two approaches may be attributed to fluorophores escaping the liquid through evaporation or by adhering to the surrounding walls. The drastic fluorescence intensity drop after the stable regime is caused by the self-quenching of fluorophores and has been reported elsewhere.[52] In other words, our results show that ~90% of the experimental process occurs at concentrations between 1 – 10 mM. Therefore, we use 2 mM dye concentration as an effort to reduce concentration effects.

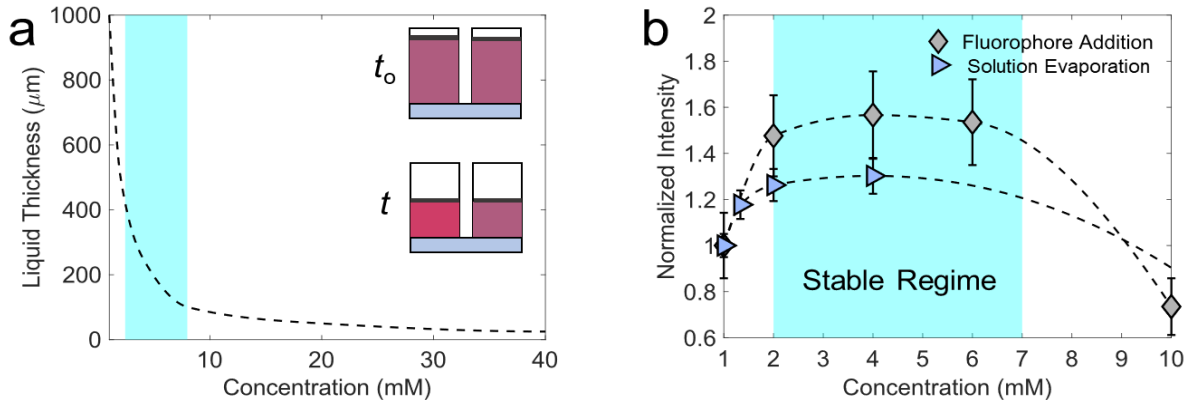

Figure 2.5: Dye concentration effects on fluorescence intensity. (a) A concentration estimation curve of an evaporating solution is plotted where the liquid thickness represents the amount of solution left. Insets show liquid thicknesses at different time frames. (b) The concentration effect on fluorescence intensity is plotted, showing the existence of a stable regime that is relatively independent of concentration between 2 – 7 mM.

2.7. Results and Discussion

To characterize the wick's evaporative performance, we measure evaporation rates at different scales using fluorescence signal tracking and fluorescence thermometry methods. For the following experiments, the sample heats up at a constant heat flux of 0.75 Wcm^{-2} with an ITO heater installed at the base of the chip. As the solution evaporates, the liquid thickness decreases and causes a reduction in fluorescence intensity. However, fluorophore residues emit a faint signal and prevents the fluorescence intensity from approaching zero even when the solution is depleted. The signals emitted from residue fluorophores are accordingly defined as the background intensity. The background-subtracted fluorescence intensity values are defined as the relative fluorescence intensity.

2.7.1 Overall Evaporation Rate

We measure the overall evaporation rate by tracking the surface fluorescence signals (i.e., surface-tracking method) of an evaporating 10 µl rhodamine B solution droplet pipetted into the wick as shown in Figure 2.6a and b. As the solution surface approaches depletion, the fluorescence intensity rapidly decreases due to liquid thickness effects (Figure 2.4b). We define the time that the relative intensity decays to 1% of its original value as the overall dry-out time t_{od}. Figure 2.6c exhibits real-time fluorescence imaging of the surface-tracking method and shows gradually growing wick features (i.e., green colored circles) along the z-axis. The presence of more solid materials at the base of the substrate causes the perceptional growth of the wick features shown in Figure 2.6c. It should be noted that the excitation light's inability to penetrate through the solid materials causes the wick structures to have low fluorescence intensity profiles. Finally, the overall evaporation rate, defined as the ratio of the evaporated mass to t_{od}, is measured as 4.44e-5 kgs^{-1}.

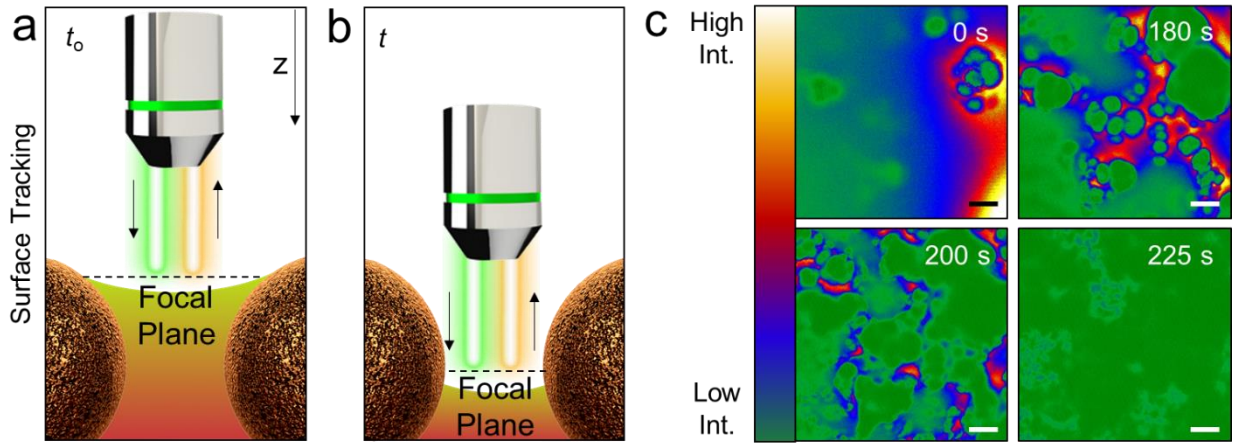

Figure 2.6: Overall evaporation rate measurement. (a-c) In the surface-tracking method, the liquid-vapor interface moves along the *z*-axis as the rhodamine B solution evaporates. The fluorescence signal emitted from the liquid-vapor interface is tracked by changing the focus plane (surface-tracking method). (a and b) The figures illustrate the surface-tracking method where (a) is the initial state and (b) is an arbitrary state during the process. The scale bar is 20 μm.

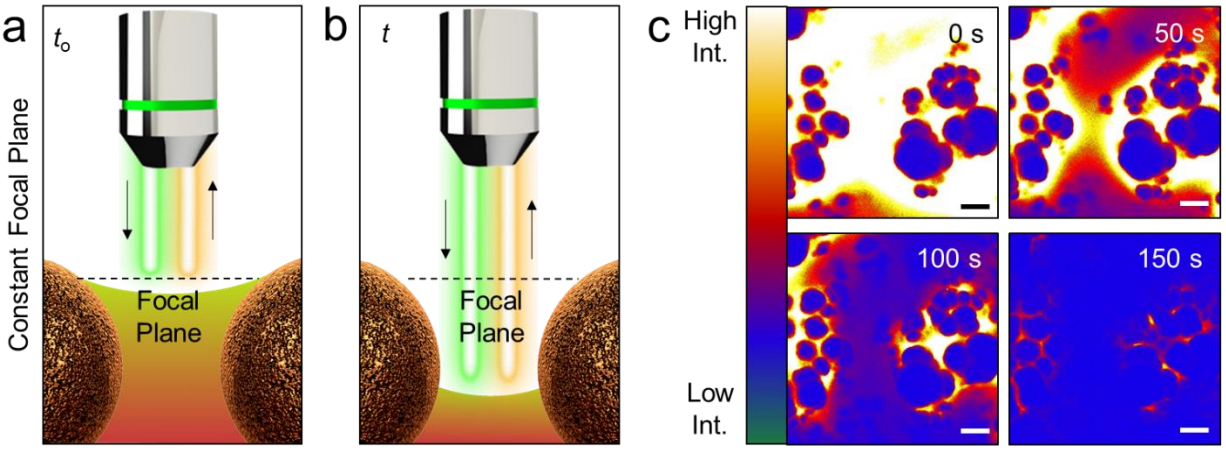

Figure 2.7: Local dry-out characterization (c) Real-time fluorescence images show the fluorescence intensity decay as the rhodamine B droplet evaporates. The scale bar represents 20 μm. (d-f) Unlike the surface-tracking method, the local evaporation rate is characterized by maintaining focus on a consistent plane (d) before and (e) during the evaporation process. (f) Temporal fluorescence images show that the fluorescence intensity decays as the solvent evaporates. The scale bar is 20 μm.

2.7.2 Local Dry-out

As an effort to untangle the strongly linked microscale phenomena that constitutes the wick's overall evaporative performance, we observe microscale (2 – 35 μm) local dry-outs. The following experiments follow the same procedures mentioned above but maintains a consistent focal plane (i.e., static focal plane), as shown in Figure 2.7a and b. Figure 2.7c shows time-dependent images of decaying fluorescence signals on a constant focal plane. In this set of experiments, the fluorescence intensity decreases as the retreating surface (or increasing focal length) impedes signal transmission. We record temporal fluorescence intensity profiles of different liquid-vapor surface areas (i.e., menisci) characterized by taking the average width (i.e., characteristic length)

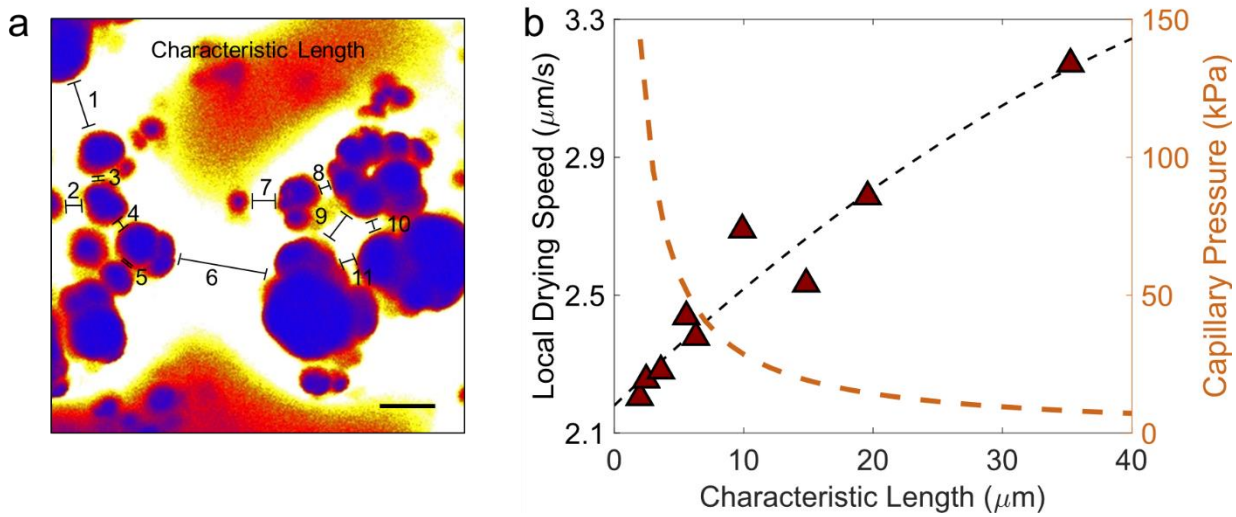

Figure 2.8: Microscale Dry-out. (a) The image shows examples of characteristic lengths of the liquid-vapor surface area between solid particles (blue color). The blue color indicates that the solid particles have low fluorescence intensity profiles which can be attributed to the inability of the excitation light to penetrate through solid materials. The scale bar is 20 μm. (b) The local drying speed shows an almost linear increasing trend with longer characteristic length, indicating that the solution dry-out occurs faster for longer characteristic lengths. The capillary pressure estimation plot based on the feature sizes show that domains with shorter characteristic lengths provide larger capillary forces.

between solid structures, as shown in Figure 2.8a. Analogous to t_{od}, the elapsed time for the relative fluorescence intensity to decrease to 1% of its original value indicates the local dry-out time t_{ld}. In addition, the local drying speed u_{ld}, which is calculated by dividing the average structural height by t_{ld} characterizes microscale dry-out. u_{ld} increases almost linearly with longer characteristic lengths, which implies that liquid confinements with larger liquid-vapor interface areas dries faster than liquid confinements with smaller surface areas (Figure 2.8b).

2.7.3 Local Evaporation Rate

We finally investigate submicron level (~0.3 μm) evaporation rates by utilizing the dye's temperature-sensitive properties. This procedure consists of three steps: (1) measuring surface fluorescence intensity of a heated solution in a steady state, (2) converting the measured fluorescence intensity to surface temperature, and (3) calculating local evaporation rates based on the obtained surface temperature profiles.

In the following experiment, a 300 μl reservoir maintains a constant liquid thickness within the porous structure upon evaporation (Figure 2.9a). The initial (i.e., cold field) (Figure 2.9b) system assumedly reaches a steady state (Figure 2.9c) when the fluorescence intensity contours remains noticeably unchanged for at least 400 seconds. Furthermore, the borderline located between the liquid and solid contours (approximately 0.3 – 1 μm from the solid contour) represents the micro regime. The fluorescence intensity are then normalized by the cold field bulk liquid surface intensity for calibration.

The local surface temperature of the bulk liquid surface and microregime is obtained by fitting the normalized fluorescence intensity values into the calibration curve in Eq. 1. The converted average

surface temperatures of the bulk liquid surface and the micro regime are 34.9ºC and 40.9ºC, respectively.

As the final step, we calculate the local evaporative mass flux by applying the converted surface temperature values into a species transport equation.[50, 53] A detailed description of the species transport mathematical model are provided in the Appendix. The obtained evaporation rates of the bulk liquid and micro regime are 7.4e-4 and 0.0011 $kgm^{-2}s^{-1}$, respectively. The results suggest that highly evaporative areas (i.e., micro regimes) form near (~0.3 – 1 μm) the solid-vapor-liquid interfaces.

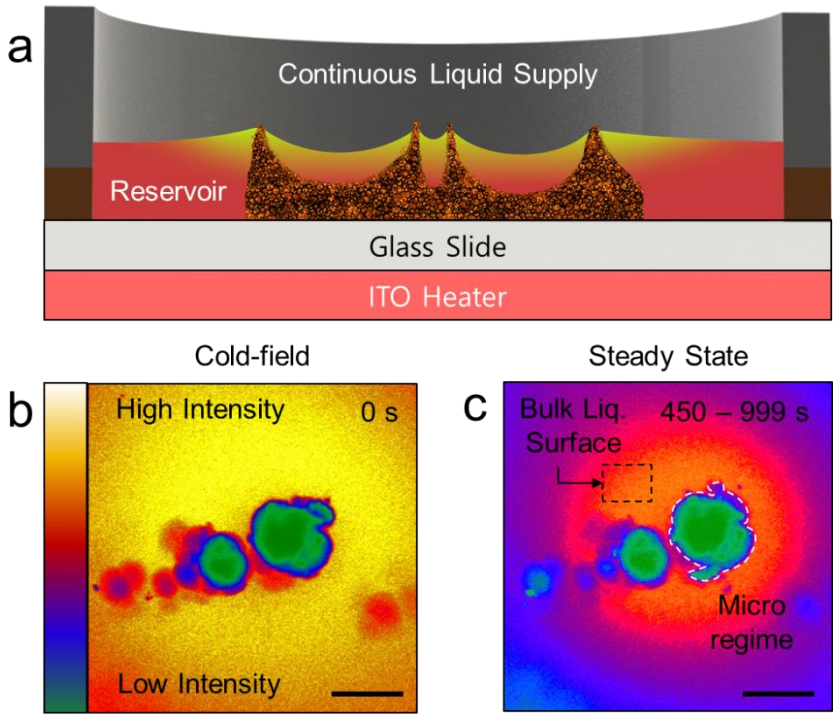

Figure 2.9: Local evaporation rate measurement. (a) A reservoir continuously supplies liquid to the wick to maintain constant liquid levels during the experiment. Average fluorescence intensities are measured for both the (b) cold-field and (c) steady state. The micro regime is visually identified by sharp fluorescence intensity-based color contrasts at the peripheral of the solid structure. The bulk liquid surface is approximately 10 μm apart from the solid particle where fluorescence intensity has a relatively uniform profile. The scale bar represents 20 μm.

2.7.4 Microscopic Liquid Pathways

Our results not only characterize overall and local evaporative phenomena but also explains passive microscopic liquid flow paths occurring within microscale structures. Based on the measured data, the micro regime exhibits a ~50% increase in evaporative mass flux (Figure 2.10a) when compared to the bulk regime. The high evaporation associated with the micro regime (also identified as the thin-film region in some papers) studies agrees with previous reports where the micro regime is found to contribute up to 80% of the overall heat transfer occurring from the entire meniscus.[12, 54, 55] A recent CFD study reports higher evaporation rates at liquid-vapor interfaces with smaller characteristic lengths.[12] In other words, liquid domains with smaller menisci have high evaporation rates because a larger portion of the menisci is influenced by the micro regime. However, we report shorter local drying speed for smaller characteristic lengths (Figure 2.8b) which may seem counterintuitive to the prior statement. We attribute this to the capillary pressure associated with different feature sizes, (Figure 2.8b). The capillary pressure

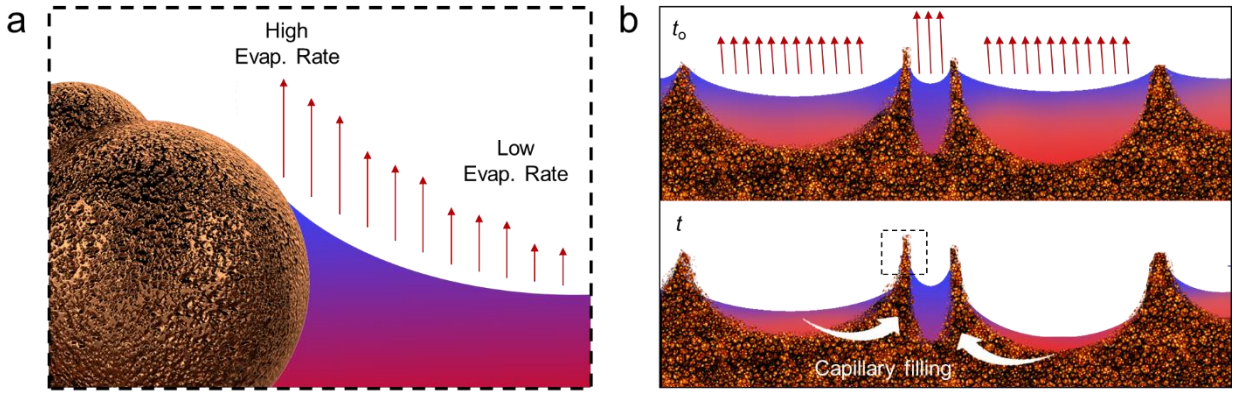

Figure 2.10: Evaporation-induced liquid flow paths within microscale structures. (a) The local evaporation rate near the liquid-vapor-solid contact line is higher than the local evaporation rate of the bulk liquid. (b) The illustrations show capillary filling into microcavities with smaller feature sizes where t_o is the initial state after liquid is wicked and t is an arbitrary state during the evaporation process.

estimation plot provided in Figure 2.8b indicates significant increases in capillary pressure as the characteristic length decreases, leading to enhanced capillary filling between smaller feature sizes. This potentially explains why smaller feature sizes can exhibit longer local drying speeds despite having higher evaporation rates as illustrated in Figure 2.10b. Since recent characterization of nanoscale meniscus pull-off forces (i.e., meniscus strength) suggests that the meniscus size can be tuned by varying heating temperatures,[37, 38] we conclude that liquids with small characteristic lengths (i.e., small meniscus) can maintain high evaporative performances by optimizing the balance between local evaporation rate (i.e., heating temperature) and capillary filling.

2.8. Conclusion

In conclusion, we analyze the local and average evaporative performances of microstructures using μLIF techniques at the submicron scales. We show the potential of employing μLIF techniques for evaporation characterizations by separating the interplaying parameters such as temperature, liquid thickness, and dye concentration of rhodamine B solutions. A series of techniques involving dynamic surface-tracking and static focal plane measurements of fluorescence signals have been demonstrated to characterize overall and local liquid dry-outs. Furthermore, we show that submicron level evaporation rates can be measured by retrieving surface temperature information converted from fluorescence signals. The integrated results infer that liquid confined between small characteristic lengths exhibits higher evaporation rates with slower drying rates. The high evaporation rate associated with small characteristic lengths is caused by the influence of the micro regime located near (~0.3 – 1 μm) the solid-vapor-liquid contact lines. The slower drying rates might be attributed to the continuous liquid supply from the vicinity through capillary feeding.

Chapter 3

Thermofluidic Characterization of Colloidal Interparticle Interactions

3.1. Introduction

Among various modern fabrication techniques, evaporative colloidal self-assembly (Figure 3.1) utilizes monodisperse nanospheres to produce crystalline templates (Figure 3.2a) which can be used to create monoporous metallic inverse opal (IO) wicks with well-defined pore diameters (Figure 3.2b).[56-62] This relatively new class of metallic architectures have been studied to exhibit large surface area-to-volume ratio and high permeability that promises enhanced energy exchange across solid-liquid and liquid-vapor interfaces.[63]

However, although the self-assembled sphere packing possesses a well-ordered crystalline arrangement at the microscale (< 100 μm), it is difficult to observe perfect colloidal crystals at the macroscale (> 100 μm) due to the creation of uncontrolled structural defects called grain boundaries (Figure 3.2c and d).[64-67] The grain boundaries are infiltrated with matter during the conversion from template to IO (Figure 3.2e and f), creating undesirable hydraulic resistances between individual grains. Eliminating or controlling the behavior of the volatile cracking phenomena during self-assembly consists of complex intermolecular physics in relation to microscale thermofluidic phenomena and therefore should be fully understood.

Recent discoveries on colloidal self-assembly suggest that grain boundaries are deeply related to saturation levels. For example, a study reported that dynamic local packings transform from FCC to BCC as the nanospheres dry.[68, 69] Based on past research, such local packing changes can

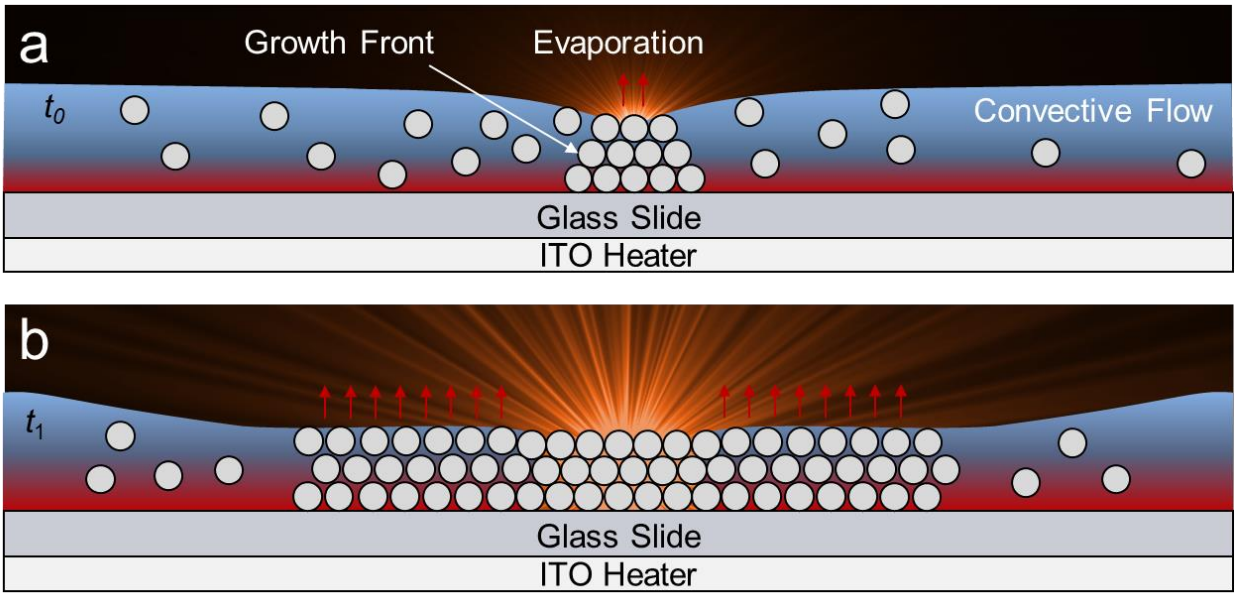

Figure 2.1: Schematic of colloidal self-assembly. (a) Particles are guided towards a growth front by evaporation-induced convective flows. An ordered structure of colloidal spheres forms as more spheres accumulate. t_o and t_1 represent different time frames. (b) As nanospheres start to assemble into crystalline opals, a relatively constant thickness film develops.

modify the entropic state of the system and trigger grain boundaries.[70] The findings mentioned above suggest that grain boundaries are byproducts of drying-induced transitional states where dynamic interparticle tension forces activate structural changes.[71, 72] Therefore, it is imperative to find a strong correlation between grain boundaries and film saturation levels; however, direct experimental measurements have been challenging due to the limited spatial resolutions of current measurement approach, which motivates us to study new high-resolution visualization techniques that can identify saturation levels during self-assembly.

In this Chapter, we employ μLIF techniques using rhodamine B to experimentally characterize real-time colloid physics during evaporative self-assembly at the submicron scale. We use an identical experimental test device and experimental setup described in Chapter 2 for all

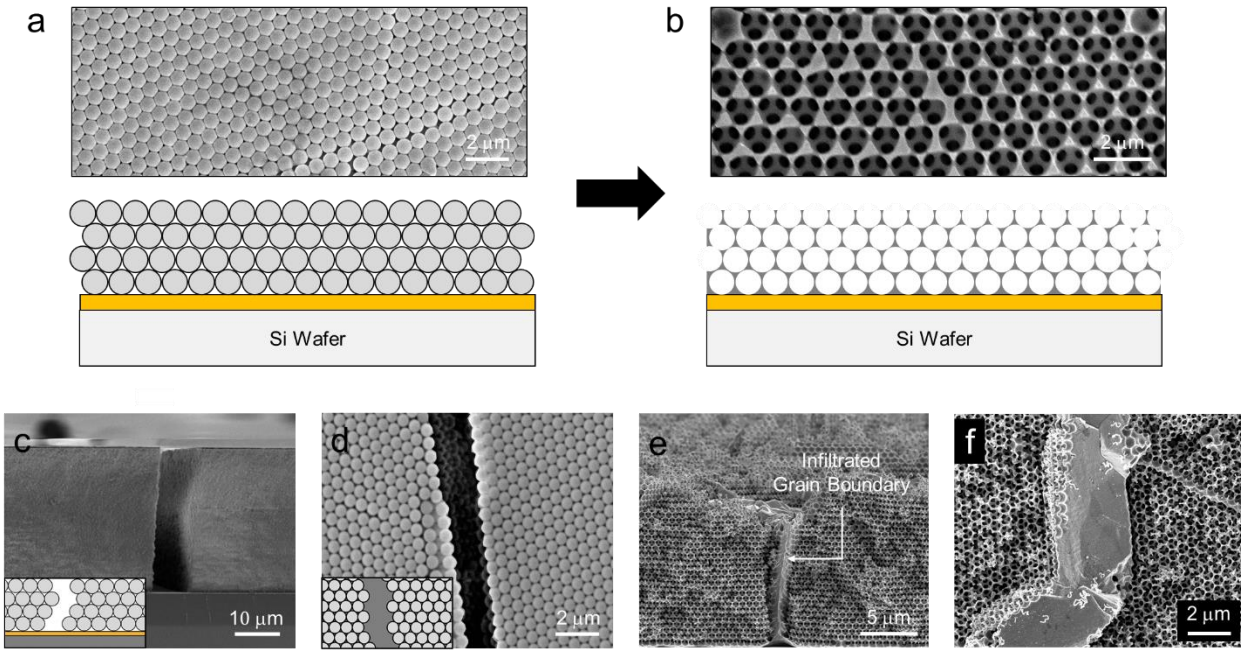

Figure 3.2: The crystalline arrangement of (a) self-assembled colloidal template and (b) inverse opal. (c) Cross-sectional and (Top) view of grain boundaries formed between nanosphere arrays are shown. The colloidal template is infiltrated with desired metallic material through conventional electrodeposition. Afterwards, the nanospheres are chemically dissolved to reveal inverse opal structures. (e) Cross-sectional and (f) top view images show grain boundaries are infiltrated with deposited material.

experiments. The fluorescence microscopy techniques are suggested to identify distinct structuring regimes dictated by their saturation levels. High-resolution measurements will allow us to examine the detailed interparticle interactions during evaporative self-assembly, resulting in the formation of grain boundaries or microcracks between crystal opals and their propagation. The crack formation and propagation physics reported in this work are valuable for studies aiming to fabricate crystalline structures with well-defined features and transport properties.

3.2. Rhodamine B and Polystyrene Latex Bead Mixture

We fabricate colloidal solutions by incorporating fluorescent dyes into polystyrene latex beads, in order to measure the level of saturation as a function of fluorescence intensity. Prior to the addition of rhodamine B (Acros Organics), a 0.1 M sodium bicarbonate buffer at pH 9.4 is prepared to ensure proper color concentration of the dye. The buffer is made with 30 ml of 0.1 M sodium carbonate and 70 ml of 0.1 M sodium bicarbonate and is diluted to 0.2 mM. Then, rhodamine B is added to the buffer solution to make a 0.1 mM fluorescence solution. The rhodamine B solutions are refined before use with a syringe filter (0.2 μm pore size). After this, monodisperse sulfate latex beads with an 8% concentration (Thermofisher Scientific, Life Technologies Corporation) and particles with 300 nm diameter are dispersed in diluted water via sonication for 20 minutes. Finally, the colloidal solution is diluted from 8% to 4% by adding rhodamine B solutions to create the RhB@PLB solution.

3.3. Fabrication of Crystalline Opal Structures

Crystalline opal structures are fabricated by drop-casting 200 μl of 4% RhB@PLB on the glass substrate of a custom self-assembly chip. After the solution is drop-casted, the solution is manually distributed using a pipette tip until the solution peripherals are in contact with the side walls of the self-assembly chamber. The indium-tin-oxide (ITO) heater on the glass substrate is heated up at a constant heat flux of 0.75 W/cm^2 by connecting with a power supply.

3.4. Results and Discussion

Self-assembly is a process by which matters form into structures through vigorous interparticle interactions and multiscale thermofluidic physics. In evaporative colloidal self-assembly,

dispersed nanospheres assemble themselves to form structures as follows: As the solvent evaporates, colloidal nanospheres start adhering to the substrate near the meniscus line, forming small organizations of packed spheres, which is denoted as the growth front (Figure 3.1a). Nearby nanospheres are driven towards the growth front via capillary-induced water flows, leading to a highly ordered, crystalline thin film (Figure 3.1b). During the structuring process, grain boundaries naturally form and propagate throughout the film. In order to understand the colloidal physics that generate grain boundaries, we explore the impact of saturation levels on the transition from dispersed nanospheres to highly ordered, crystalline thin films by using μLIF techniques (Figure 1.2). The μLIF techniques enable real-time observation of saturation levels by tracking the fluorescence intensity of the mixture of rhodamine B and polystyrene latex beads (hereafter denoted as RhB@PLB).

3.4.1 Characterization of Rhodamine B and Polystyrene Latex Bead Mixture

The evaporation phenomena during the self-assembly process impact the overall RhB@PLB's fluorescence intensity in relation to the combination of the medium thickness and the number of fluorophores per unit volume (i.e., local dye concentration). The dynamic medium thickness influences the fluorescence intensity by dictating the dye-incorporated media volume the excitation light passes through,[73] which means the fluorescence intensity decreases with smaller medium thickness. The initial solution state has excess solvent with respect to spheres and the overall fluorescence intensity is thereby mainly dominated by the evaporation. It should be noted that the medium thickness becomes relatively constant if the solvent level is below the film thickness of packed nanospheres. (Figure 3.1b). In addition, the number of fluorophore particles loaded onto nanospheres increases, and the mean distance between doped particles decreases, as

the solvent evaporates. This all consequentially increases the local dye concentration and fluorescence intensity, as illustrated in Figure 3.3. A detailed description of the fluorescence

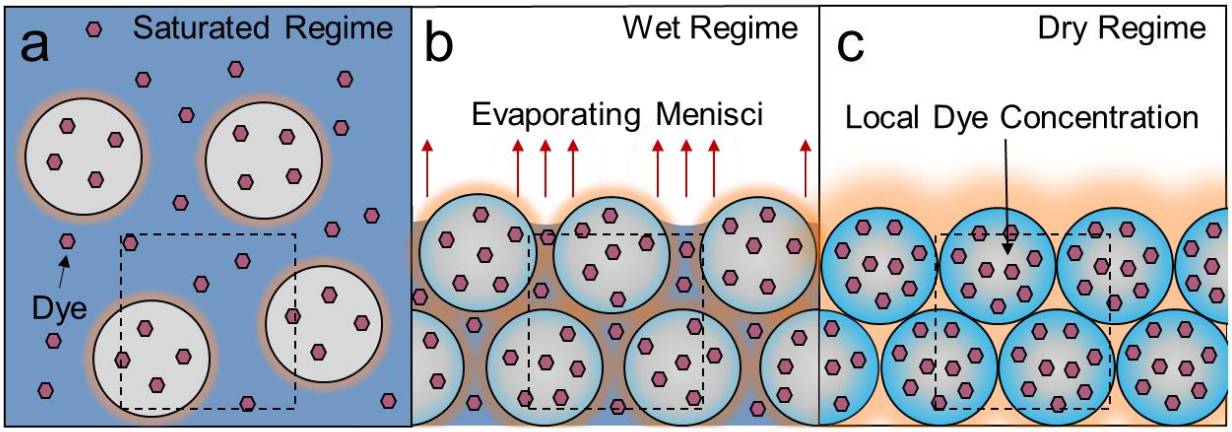

Figure 3.3: (a-c) The number of dye particles loaded onto colloidal particles and mean distances between doped particles dictates the saturation level of the film and thereby the fluorescence intensity.

intensity-saturation level relationship of RhB@PLB is provided in the Appendix. Since the medium thickness effect is negligible when the nanospheres begin to assemble into films, we hypothesize that the fluorescence intensity is mainly governed by the solvent saturation levels in this study. A constant sphere size and colloidal concentration of 300 nm and 4%, respectively, is selected.

3.4.2 Dynamic Structing Regimes Governed by Film Saturation Level

To validate the hypothesis described above, we characterize the real-time self-assembly process by identifying different regimes — 1) the saturated regime, 2) the wet regime, and 3) the dry regime (Figure 3.4). The saturated regime (Figure 3.4a) describes the state before nanosphere structuring. The excess solvent in the saturated regime allows both dye and nanosphere particles to move

throughout the solution with relatively long interparticle distances that result in weak fluorescence signals (Figure 3.4e). As the solvent evaporates, the nanospheres organize themselves into a loosely packed configuration, called the wet regime (Figure 3.4b-c). The fluorescence intensity-based image in Figure 3.4a shows the wet regime expanding through the saturated regime where the fluorescence intensity increases by approximately 44% (Figure 3.4e). The quick transition (~15

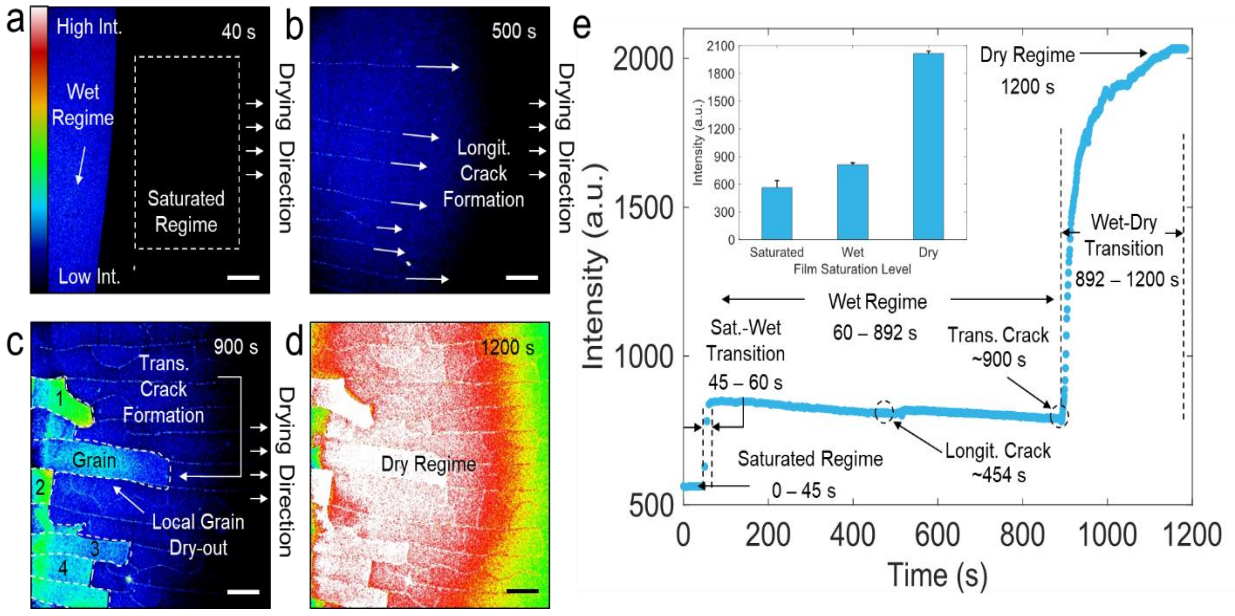

Figure 3.4: Distinctive saturation regimes during evaporative self-assembly. (a) The image shows the wet regime expanding through the saturated regime. (b) As the wet regime expands, cracks initiate and propagate in the drying direction (i.e., longitudinal cracks), which are indicated by arrows. (c) At a later stage, cracks perpendicular to the drying direction (i.e., transverse cracks) form and create an isolated domain (i.e., grain). The opal film dries in discrete steps as local grain dry-out occurs. Individual grains are identified with numbers for the dry-out analysis in Figure 4. (d) The fluorescence intensity abruptly increases after the complete dry-out. The scale bars represent 100 μm. (e) The average fluorescence intensity of the dashed box in (a) shows stepwise increases with time. Each step represents a different saturation regime (e.g., saturated regime, wet regime, and dry regime). The inset shows the average intensity of each saturation regime.

s) from the saturated regime to the wet regime indicates rapid nanosphere assembly. The wet regime remains at a relatively constant intensity for 832 s, suggesting that the overall structure's saturation level is preserved during this process. The constant saturation level can be explained by a continuous water flow via capillary wicking from the bulk solution to the growth front. It should be mentioned that minor photobleaching (2% - 9%) occurs during the wet regime as the film is exposed to the laser for a relatively long time. Finally, the solvent completely evaporates, which stops further liquid delivery, leading to the dry-out domains in the dry regime (Figure 3.4d). The transition from the wet to the dry regime is easily identified by an increase in the fluorescence intensity by ~153%, as shown in Figure 3.4e.

3.4.3 Fundamental Investigation of Longitudinal Cracking Mechanism

While the overall saturation level measurements reveal the transition between the different regimes during colloidal self-assembly, it is critical to identify local saturation levels to understand cracking phenomena with a high spatial resolution (Figure 3.5). The longitudinal cracks first develop in the drying direction (Figure 3.4b), followed by the formation of the transverse cracks in later steps. Furthermore, longitudinal cracks develop in the wet regime where the active assembly of nanospheres starts forming packed structures; as the wet regime expands, the cracks propagate further by tensile stresses accumulated within the film. The propagation of a single longitudinal crack through the film as well as the differences in local saturation levels are confirmed by time-dependent, high-magnification μLIF images in Figure 3.5a-c.The crack peripherals (denoted as the near-crack domain) emit higher fluorescence intensity when compared to the rest of the bulk film (denoted as the opal domain), as plotted in Figure 3.5d. Furthermore, the black and red lines in Figure 3.5e show the average fluorescence intensity of opal and near-crack domain, respectively,

as the regime transforms from the wet to the dry regime. In the wet regime, the difference in average fluorescence intensity between the opal domain and the near-crack domain remains relatively constant. However, the difference in the average fluorescence intensity gradually diminishes as the film dries. This means that the near-crack domain is drier than the opal domain during the wet regime.

The saturation level difference between the opal domain and the near-crack domain can be explained by the capillary-assisted evaporation after grain boundary formation. Figure 3.5g-l illustrates the front and top view cracking schematics, where the blue and grey spheres represent dry and wet nanospheres, respectively. Before cracks are introduced to the film, the evaporating menisci is primarily located at the top of the sphere array, as shown in Figure 3.5j. As longitudinal cracks steadily propagate through the film and generate gaps between the packed spheres (Figure 3.5g and h), water flux comes from the crack area to the organized spheres through the capillary-assisted wicking and creates additional evaporative surfaces, as illustrated in Figure 3.5k. Therefore, capillary-assisted evaporation occurs at the near-crack and causes the near-crack domain to dry faster (Figure 3.5h and k). Eventually the opal film consisting of packed spheres completely dries, as illustrated in Figure 3.5i and l.

The differences in the saturation levels between the opal domain and the near-crack domain in the wet regime are identified by defining a “normalized dryness (ND),” which is the ratio of fluorescence intensity to the average fluorescence intensity of the dry regime. The ND of the near-crack domain (ND = 0.5) is approximately 25% higher than that of the opal domain (ND = 0.4) where the dry regime ND =1. This result quantitatively indicates that the near-crack domain is

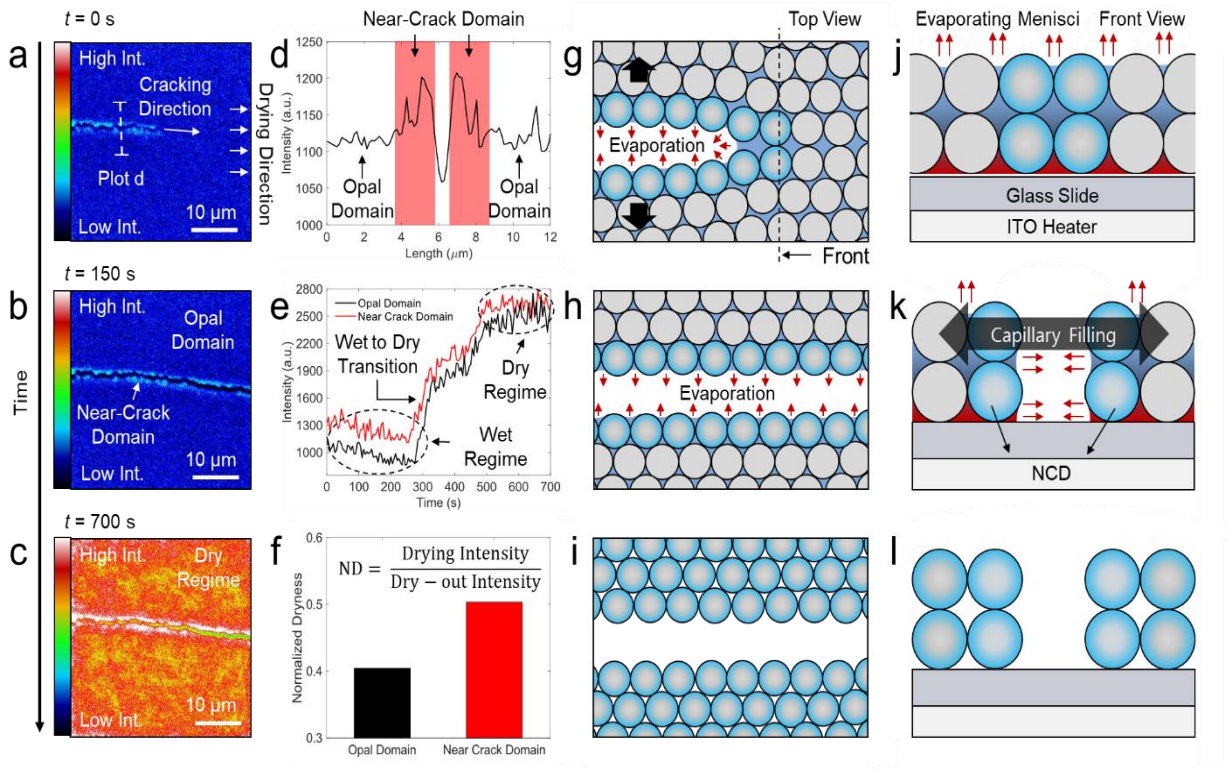

Figure 3.5: Crack formation and propagation phenomena associated with the local evaporation. (a-c) High magnified fluorescence images show a longitudinal crack propagating through the film. (a) The drying direction and cracking direction are shown. (b) The opal domain and the near-crack domain is indicated in the figure. (c) Dry-out causes the fluorescence intensity to drastically increase. (d) The fluorescence intensity profile of the dashed line drawn in (a) exhibits high intensities at the near-crack domain (red block). The abrupt dip in fluorescence intensity is caused by the absence of solution at the fissure caused by the crack. (e) Time-dependent plots of the opal and the near-crack domains show fluorescence intensity differences between the two domains decreases as the film dries. (f) The normalized dryness shows that the near-crack domain has a ~25% higher fluorescence intensity than the opal domain during the wet regime, which indicates a lower saturation level. The crack formation and propagation associated with local evaporation phenomena are illustrated from the (g-i) top and (j-l) front view. The blue and grey color represent dry and wet nanospheres, respectively.

drier than the opal domain.

The results suggest that evaporation rate misbalances between the opal domain and the near-crack domain expediate the longitudinal crack propagation. The evaporation rate misbalances between the opal domain and the near-crack domain can generate auxiliary drying-induced tension forces in the transverse direction, which would encourage longitudinal cracking.

3.4.4 Transverse Crack Formation and Local Grain Dry-Out

Transverse cracks – the cracks that develop normal to the drying direction - form due to force misbalances within the film, which is similar to longitudinal cracks. However, unlike longitudinal cracks (Figure 3.6a), transverse cracks consume less time to fully develop due to their short lengths and usually develop at a later stage (Figure 3.6b). A set of both longitudinal and transverse cracks creates an isolated opal domain, called the crystal grain or the grain. With this in mind, the drying process of the overall film can be considered as a comprehensive drying of individual grains over time (i.e., local grain dry-out).

μLIF observations reveal that individual grains dry in a systematic, step-by-step procedure driven by microscopic liquid transport phenomena. Figure 3.6c represents *in situ* saturation levels of individual grains numbered in Figure 3.4c. The measurement starts when the first longitudinal cracks appear in the visualization window at t = 454 s and ends when the film fully dries at t = 1200 s. The multiple stepwise fluorescence intensity jumping in Figure 3.6c indicate asynchronous drying in local film areas (i.e., grains). The intensity discrepancies of individual grains upon dry-out (~t = ~1200 s) in Figure 3.6c are attributed to grain lift-off effects, explained in the Appendix. Interestingly, the fluorescence intensity in Figure 3.6c jumps immediately after the formation of transverse cracks while remaining unchanged during the longitudinal crack's earlier development.

This phenomena can be explained by selective capillary-assisted liquid transport from the bulk liquid to the grains. As noted in previous sections, the presence of the nanoscale pores between packed spheres enables liquid feeding from the bulk solution to the growth front via capillary wicking. However, grain boundaries work as hydraulic resistances as the liquid in the created grain boundaries is quickly absorbed by the surrounding opal structures (Figure 3.5k). Therefore, grain boundaries can create innately different liquid transport impediments depending on their propagation direction. On the one hand, the longitudinal cracks have minimum impact on liquid transport because they are in alignment with the direction of the liquid supply (Figure 3.6a). On the other hand, the transverse crack creates a gap in a direction that impedes capillary feeding (Figure 3.6b). The hydraulic resistances along the liquid feeding originated from the transverse cracks facilitate local grain dry-outs, which results in non-simultaneous film dry-out.

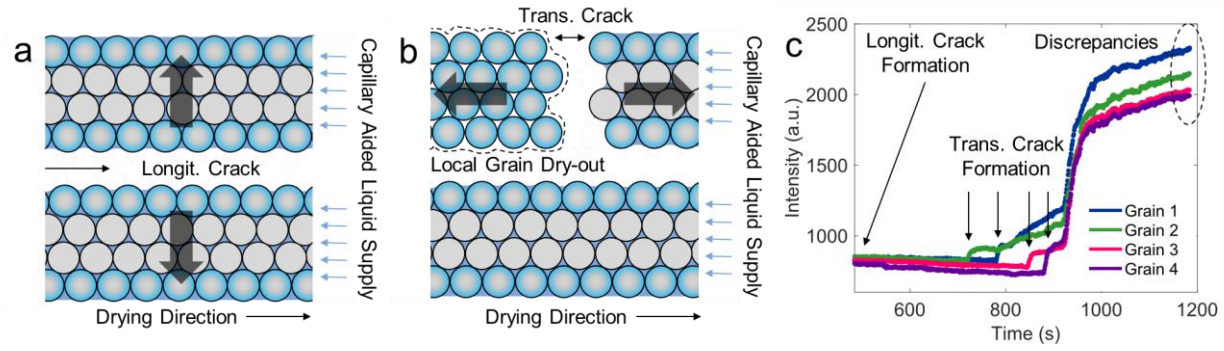

Figure 3.6: Grain dry-out mechanism. (a) As longitudinal cracks form, the separated structures are continuously supplied with liquid via capillary wicking. Longitudinal cracks form due to tensile forces (indicated in black arrows) in the direction perpendicular to the drying direction. On the other hand, (b) transverse cracks form due to tensile forces parallel to the drying direction (indicated in black arrows). Transverse cracks prevents further liquid supply to the isolated structure (i.e., grain), which leads to local grain dry-out. (c) The average intensity of individual grains in Figure 2c displays a stepwise increase right after transverse cracks form. The arrows indicate when longitudinal and transverse cracks start to form.

3.5. Conclusion

In summary, we employ a novel μLIF technique that overcomes extant resolution barriers to experimentally characterizes real-time interparticle interactions in colloidal assemblies that decide grain boundary formation mechanisms with up to 300 nm spatial resolution. Our method identifies three distinctive saturation level-dictated structuring phases called the saturated, the wet, and the dry regime. The fluorescence intensity increases by 44% and 153% during saturated to wet regime and wet to dry regime transition, respectively. The saturation level jumps indicate discrete saturation level reductions during the self-assembly process. The quick transition (~15 s) from saturated to wet regime suggest a rapid structuring of nanospheres. In addition, grain boundaries form in the wet regime where the local saturation level measurements shows that the near-crack domain has 25% lower normalized dryness than the opal domain, suggesting the existence of microscale evaporation rate misbalances between the two domains. The evaporation rate misbalances in turn can cause auxiliary tensile forces that especially promote longitudinal cracks. Furthermore, *in situ* saturation level monitoring shows that transverse cracks function as hydraulic barriers that trigger local grain dry-out, which eventuate in non-simultaneous film dry-out.

Chapter 4

Conclusion and Future Work

This thesis provides fundamental understanding of the thermofluidic transport phenomena occurring within porous media. The findings in this study address the challenge of designing and fabricating an improved wicking structure for phase-change thermal management devices.

4.1. Summary of Work

We systematically measure multiscale evaporation rates through high resolution analysis of the thermofluidic transport phenomena. To overcome extant experimental resolution barriers, we develop a novel μLIF technique that considers temperature, liquid thickness, and concentration effects on fluorescence intensity. For submicron level characterization, vapor transport equations are employed to calculate evaporation rates based on fluorescence intensity to temperature calibrations. Unlike traditional studies, our results help decompose key physical parameters such as microscopic liquid flow paths that influence the wick's evaporative performance. We demonstrate that the balance between capillary-assisted liquid feeding and thin-film evaporation determines local drying rates in wick structures.

We also extend the use of the μLIF technique to study *in situ* interparticle interactions in colloidal assemblies with the aim to investigate thermofluidic physics that decide cracking mechanics during evaporative colloidal self-assembly. The results suggest that grain boundaries are determined by dynamic colloidal structuring regimes governed by the film's saturation level. A closer examination of the saturation levels shows that capillary-assisted wicking and

corresponding spatial evaporation misbalances promote longitudinal grain boundaries, while transverse grain boundaries function as hydraulic barriers that trigger local grain dry-out. The findings in this study promise innovational advances in large scale fabrication of self-assembled templates used for IO wicks.

4.2. Future Work

Further work is needed to elucidate the medium thickness effects caused by liquid-vapor interface shapes on fluorescence intensity described in Chapter 2. For local evaporation rate measurements explained in 2.7.3, acquiring liquid-vapor interface shapes between local sub-micron features is are crucial in collecting accurate surface temperature profiles. The random, tortuous nature of the biporous copper wick obscures sideview visualization and complicates experimental or computational meniscus shape regeneration. For simplification, we assume the influence of microscopic liquid thickness variations caused by the liquid-vapor interface between the microstructures is relatively small compared to that of bulk liquid thickness. Nevertheless, obtaining an accurate liquid-vapor interface model will provide a better understanding of the geometrical features of the meniscus and therefore help define a more robust micro regime. With our definition, we acquire a relatively large temperature difference (~6^{o}C) between the micro regime and the bulk liquid. To address these limitations, future work will include a more reliable analysis of the meniscus shape and its effect on fluorescence intensity by utilizing controlled microstructures such as micropillars.

The μLIF technique presented in this study shows potential to be developed for advanced sensing technology. For example, our μLIF techniques demonstrate high sensitivity and reversibility to saturation levels as shown in the Appendix, which might be useful to detect unintentional local

dry-out locations in microfluidic channels. In addition, the techniques might have potential to be exploited as *in situ* stress measurement tools. As future work, we will investigate the correlation between interparticle saturation levels and particle distances to derive quantitative measurements for drying-induced tensile stresses in thin films.

Bibliography

1. Rupp, K. In *40 years of microprocessor trend data*, GitHub, **2018**.
2. Pop, E., *Nano Res* **2010,** *3* (3), 147-169. DOI 10.1007/s12274-010-1019-z.
3. Rupp, K.; Horovitz, M.; Labonte, F.; Shacham, O.; Olukotun, K.; Hammond, L.; Batten, C., *by karlrupp. net.[Online*.
4. Thome, J. R., *Heat Transfer Eng* **2006,** *27* (9), 1-3. DOI 10.1080/01457630600845283.
5. Mahajan, R.; Chiu, C. P.; Chrysler, G., *P Ieee* **2006,** *94* (8), 1476-1486. DOI 10.1109/Jproc.2006.879800.
6. Lu, M.-C. Exploring the limits of boiling and evaporative heat transfer using micro/nano structures. UC Berkeley, **2010**.
7. Pham, Q. N.; Suh, Y.; Shao, B.; Won, Y. In *Boiling Heat Transfer Using Spatially-Variant and Uniform Microporous Coatings*, ASME 2019 International Technical Conference and Exhibition on Packaging and Integration of Electronic and Photonic Microsystems, American Society of Mechanical Engineers Digital Collection.
8. Zhu, Y. Y.; Antao, D. S.; Chu, K. H.; Chen, S. Y.; Hendricks, T. J.; Zhang, T. J.; Wang, E. N., *J Heat Trans-T Asme* **2016,** *138* (9). DOI Artn 091501
10.1115/1.4033497.
9. Singh, P. K.; Sahu, S. K.; Upadhyay, P. K.; Jain, A. K., *Appl Therm Eng* **2020,** *165*. DOI ARTN 114596
10.1016/j.applthermaleng.2019.114596.
10. Zhao, X.; Zhang, B.; Yang, Z. G.; Zhao, Y. X., *Int J Heat Mass Tran* **2020,** *147*. DOI ARTN 118960
10.1016/j.ijheatmasstransfer.2019.118960.
11. Montazeri, K.; Zhang, S. W.; Qomi, M. J. A.; Won, Y., *Intsoc Conf Thermal* **2018**, 470-476.
12. Montazeri, K.; Lee, H.; Won, Y., *Int J Heat Mass Tran* **2018,** *122*, 59-68. DOI 10.1016/j.ijheatmasstransfer.2018.01.002.
13. Faghri, A. J. J. o. h. t., **2012,** *134* (12), 123001.
14. Launay, S.; Sartre, V.; Bonjour, J., *Int J Therm Sci* **2007,** *46* (7), 621-636. DOI 10.1016/j.ijthermalsci.2006.11.007.
15. Yeh, C. C.; Chen, C. N.; Chen, Y. M., *Int J Heat Mass Tran* **2009,** *52* (19-20), 4426-4434. DOI 10.1016/j.ijheatmasstransfer.2009.03.059.
16. Weisenseel, B.; Greil, P.; Fey, T. J. A. E. M., **2017,** *19* (1), 1600379.
17. Huminic, G.; Huminic, A.; Morjan, I.; Dumitrache, F., *Int J Heat Mass Tran* **2011,** *54* (1-3), 656-661. DOI 10.1016/j.ijheatmasstransfer.2010.09.005.
18. Lee, J.; Suh, Y.; Dubey, P. P.; Barako, M. T.; Won, Y., *Acs Appl Mater Inter* **2019,** *11* (1), 1546-1554. DOI 10.1021/acsami.8b14955.
19. Bodla, K. K.; Weibel, J. A.; Garimella, S. V., *J Heat Trans-T Asme* **2013,** *135* (6). DOI Artn 061202
10.1115/1.4023569.
20. Kandlikar, S. G., *J Heat Trans-T Asme* **2017,** *139* (5). DOI Artn 051501
10.1115/1.4035247.

21. Li, T.; Peterson, G. P., *J Heat Trans-T Asme* **2006,** *128* (12), 1320-1328. DOI 10.1115/1.2349508.
22. Ranjan, R.; Murthy, J. Y.; Garimella, S. V.; Vadakkan, U.; Transfer, M., *Int J Heat Mass Transfer* **2011,** *54* (1-3), 153-168.
23. Wen, R. F.; Li, Q.; Wang, W.; Latour, B.; Li, C. H.; Li, C.; Lee, Y. C.; Yang, R. G., *Nano Energy* **2017,** *38*, 59-65. DOI 10.1016/j.nanoen.2017.05.028.
24. Li, J. Q.; Fu, W. C.; Zhang, B. H.; Zhu, G. H.; Miljkovic, N., *Acs Nano* **2019,** *13* (12), 14080-14093. DOI 10.1021/acsnano.9b06501.
25. Suh, Y.; Pham, Q.; Shao, B. W.; Won, Y., *Small* **2019,** *15* (12). DOI ARTN 1804523 10.1002/smll.201804523.
26. Mishan, Y.; Mosyak, A.; Pogrebnyak, E.; Hetsroni, G., *International Journal of Heat and Mass Transfer* **2007,** *50* (15-16), 3100-3114. DOI 10.1016/j.ijheatmasstransfer.2006.12.003.
27. Carlomagno, G. M.; Cardone, G., *Experiments in Fluids* **2010,** *49* (6), 1187-1218. DOI 10.1007/s00348-010-0912-2.
28. Girard, F.; Antoni, M.; Sefiane, K., *Langmuir* **2010,** *26* (7), 4576-4580. DOI 10.1021/la9048659.
29. Christofferson, J.; Maize, K.; Ezzahri, Y.; Shabani, J.; Wang, X.; Shakouri, A., *2007 International Conference on Thermal Issues in Emergingtechnologies - Theory and Applications* **2007**, 3-+. DOI Doi 10.1109/Theta.2007.363399.
30. Dhavaleswarapu, H. K.; Garimella, S. V.; Murthy, J. Y., *J Heat Trans-T Asme* **2009,** *131* (6). DOI Artn 061501 10.1115/1.3090525.
31. Low, P.; Kim, B.; Takama, N.; Bergaud, C., *Small* **2008,** *4* (7), 908-914. DOI 10.1002/smll.200700581.
32. Hohmann, C.; Stephan, P., *Experimental Thermal and Fluid Science* **2002,** *26* (2-4), 157-162. DOI Pii S0894-1777(02)00122-X Doi 10.1016/S0894-1777(02)00122-X.
33. Kenning, D. B. R.; Yan, Y. Y., *Int J Heat Mass Tran* **1996,** *39* (15), 3117-&. DOI Doi 10.1016/0017-9310(96)00006-3.
34. Ekkad, S. V.; Han, J. C., *Meas Sci Technol* **2000,** *11* (7), 957-968. DOI Doi 10.1088/0957-0233/11/7/312.
35. Brites, C. D. S.; Lima, P. P.; Silva, N. J. O.; Millan, A.; Amaral, V. S.; Palacio, F.; Carlos, L. D., *Nanoscale* **2012,** *4* (16), 4799-4829. DOI 10.1039/c2nr30663h.
36. Tovee, P. D.; Kolosov, O. V., *Nanotechnology* **2013,** *24* (46). DOI Artn 465706 10.1088/0957-4484/24/46/465706.
37. Assy, A.; Gomes, S., *Nanotechnology* **2015,** *26* (35). DOI Artn 355401 10.1088/0957-4484/26/35/355401.
38. Wilson, A. A.; Sharar, D. J., *Intsoc Conf Thermal* **2018**, 240-245.
39. Martinek, J.; Klapetek, P.; Campbell, A. C., *Ultramicroscopy* **2015,** *155*, 55-61. DOI 10.1016/j.ultramic.2015.04.011.
40. Menges, F.; Mensch, P.; Schmid, H.; Riel, H.; Stemmer, A.; Gotsmann, B., *Nature Communications* **2016,** *7*. DOI ARTN 10874 10.1038/ncomms10874.
41. Rochlitz, H.; Scholz, P., *Experiments in Fluids* **2018,** *59* (3). DOI ARTN 54 10.1007/s00348-018-2508-1.

42. Volkov, R. S.; Strizhak, P. A., *Applied Thermal Engineering* **2017,** *127*, 141-156. DOI 10.1016/j.applthermaleng.2017.08.040.
43. Chaze, W.; Caballina, O.; Castanet, G.; Lemoine, F., *Experiments in Fluids* **2017,** *58* (8). DOI ARTN 96
10.1007/s00348-017-2375-1.
44. Feng, J.; Xiong, L.; Wang, S. Q.; Li, S. Y.; Li, Y.; Yang, G. Q., *Adv Funct Mater* **2013,** *23* (3), 340-345. DOI 10.1002/adfm.201201712.
45. Erickson, D.; Sinton, D.; Li, D. Q., *Lab on a Chip* **2003,** *3* (3), 141-149. DOI 10.1039/b306158b.
46. Samy, R.; Glawdel, T.; Ren, C. L., *Anal Chem* **2008,** *80* (2), 369-375. DOI 10.1021/ac071268c.
47. Glawdel, T.; Almutairi, Z.; Wang, S.; Ren, C., *Lab on a Chip* **2009,** *9* (1), 171-174. DOI 10.1039/b805172k.
48. Ross, D.; Gaitan, M.; Locascio, L. E., *Analytical Chemistry* **2001,** *73* (17), 4117-4123. DOI 10.1021/ac010370l.
49. Vetrone, F.; Naccache, R.; Zamarron, A.; de la Fuente, A. J.; Sanz-Rodriguez, F.; Maestro, L. M.; Rodriguez, E. M.; Jaque, D.; Sole, J. G.; Capobianco, J. A., *Acs Nano* **2010,** *4* (6), 3254-3258. DOI 10.1021/nn100244a.
50. Feng, J.; Tian, K. J.; Hu, D. H.; Wang, S. Q.; Li, S. Y.; Zeng, Y.; Li, Y.; Yang, G. Q., *Angew Chem Int Edit* **2011,** *50* (35), 8072-8076. DOI 10.1002/anie.201102390.
51. Suh, Y.; Lin, C.-H.; Gowda, H.; Won, Y. In *Evaporation Rate Measurement at Multiple Scales Using Temperature-Sensitive Fluorescence Dyes*, ASME 2019 International Technical Conference and Exhibition on Packaging and Integration of Electronic and Photonic Microsystems, American Society of Mechanical Engineers Digital Collection.
52. Fikry, M.; Omar, M. M.; Ismail, L. Z., *Modern Trends in Physics Research: Third International Conference on Modern Trends in Physics Research* **2011**, 210-219.
53. Pan, Z. H.; Dash, S.; Weibel, J. A.; Garimella, S. V., *Langmuir* **2013,** *29* (51), 15831-15841. DOI 10.1021/la4045286.
54. Wang, H.; Garimella, S. V.; Murthy, J. Y., *Int J Heat Mass Tran* **2007,** *50* (19-20), 3933-3942. DOI 10.1016/j.ijheatmasstransfer.2007.01.052.
55. Bodla, K. K.; Murthy, J. Y.; Garimella, S. V., *Int J Heat Mass Tran* **2013,** *61*, 729-741. DOI 10.1016/j.ijheatmasstransfer.2013.02.038.
56. Holgado, M.; Garcia-Santamaria, F.; Blanco, A.; Ibisate, M.; Cintas, A.; Miguez, H.; Serna, C.; Molpeceres, C.; Requena, J.; Mifsud, A. J. L., *Langmuir* **1999,** *15* (14), 4701-4704.
57. Jiang, P.; McFarland, M. J., *J Am Chem Soc* **2004,** *126* (42), 13778-13786.
58. KrishnaáKaruturi, S.; TatáSu, L.; KueiáChan, T.; Tok, A. I., *J Nanoscale* **2011,** *3* (12), 4951-4954.
59. Liu, G.; Zhou, L.; Wu, Y.; Wang, C.; Fan, Q.; Shao, J., *J Appl Polym Sci* **2015,** *132* (13).
60. Meijer, J.-M.; Hagemans, F.; Rossi, L.; Byelov, D. V.; Castillo, S. I.; Snigirev, A.; Snigireva, I.; Philipse, A. P.; Petukhov, A. V., *Langmuir* **2012,** *28* (20), 7631-7638.
61. Shao, J.; Zhang, Y.; Fu, G.; Zhou, L.; Fan, Q., *J Text Inst* **2014,** *105* (9), 938-943.
62. Zhou, Z.; Zhao, X., *Langmuir* **2005,** *21* (10), 4717-4723.
63. Pham, Q.; Barako, M.; Tice, J.; Won, Y. J. S. R., **2017,** *7* (1), 10465.
64. Wong, S.; Kitaev, V.; Ozin, G. A., *J Am Chem Soc* **2003,** *125* (50), 15589-15598.
65. Teh, L.; Tan, N.; Wong, C.; Li, S., *J Appl Phys A* **2005,** *81* (7), 1399-1404.

66. Liu, G.; Wang, Z.; Ji, Y., *Thin Solid Films* **2010,** *518* (18), 5083-5090.
67. Ye, Y.-H.; LeBlanc, F.; Haché, A.; Truong, V.-V., *J Appl Phys Lett* **2001,** *78* (1), 52-54.
68. Lokteva, I.; Koof, M.; Walther, M.; Grubel, G.; Lehmkuhler, F., *Small* **2019,** *15* (20), e1900438. DOI 10.1002/smll.201900438.
69. Weidman, M. C.; Smilgies, D. M.; Tisdale, W. A., *Nature Materials* **2016,** *15* (7), 775-+. DOI 10.1038/Nmat4600.
70. Manoharan, V. N., *Science* **2015,** *349* (6251). DOI ARTN 1253751 10.1126/science.1253751.
71. Woodcock, L., *Nature* **1997,** *385* (6612), 141.
72. Dziomkina, N. V.; Hempenius, M. A.; Vancso, G. J., *Polymer* **2009,** *50* (24), 5713-5719.
73. Greszik, D.; Yang, H.; Dreier, T.; Schulz, C., *Applied Physics B-Lasers and Optics* **2011,** *102* (1), 123-132. DOI 10.1007/s00340-010-4200-x.

Appendix : Mathematical Model

In section 2.8.3, we calculate local evaporation rates based on surface temperatures by employing a species transport equation for vapor at the liquid-vapor interface. By assuming that the equilibrium vapor pressure at the interface $p_{v\_equ}(T_{lv})$ is equivalent to the saturation pressure, the Clausius-Clapeyron equation provides an expression for the saturation pressure $p_{sat}(T_{lv})$:

$$p_{v\_equ}(T_{lv}) \approx p_{sat}(T_{lv}) = p_{sat\_ref}(T_{lv}) \exp\left(\frac{Mh_{fg}}{R}\left(\frac{1}{T_{sat\_ref}} - \frac{1}{T_{lv}}\right)\right) \quad (A.1)$$

where $p_{sat\_ref}(T_{lv})$ is the reference saturation pressure of 1 atm, M is the vapor molecular weight, h_{fg} is the latent heat, T_{sat_ref} is the reference saturation temperature at 1 atm, R is the universal gas constant, and T_{lv} is the liquid-vapor temperature. On the other hand, the mass flux (i.e., evaporative mass flux $\dot{m}''$) at the liquid-vapor interface is provided through a general species transport equation:

$$\dot{m}_v'' = M(-D\vec{n} \cdot \nabla C_v + u_n C_v) \quad (A.2)$$

where D is the diffusion coefficient, u is the fluid velocity, and C is the molar concentration. A similar equation can be written for air. Since there is no mass transport of air ($\dot{m}_{air}'' = 0$) through the interface, the species transport equation for air becomes:

$$u_n|_{lv} = \frac{D}{C_{air}}(\vec{n} \cdot \nabla C_{air})|_{lv} \quad (A.3)$$

$$= -\frac{D}{C_{tot} - C_v}(\vec{n} \cdot \nabla C_v)|_{lv} \quad (A.4)$$

By substituting this to Eq. A.2:

$$\dot{m}_v^{"} = -\frac{MD}{1 - {C_v}/{C_{tot}}}(\vec{n} \cdot \nabla C_v)|_{lv} \quad (A.5)$$

According to the ideal-gas law:

$$C_{tot}|_{lv} = \frac{p_{atm}}{RT_{lv}} \quad (A.6)$$

$$C_v|_{lv} = \frac{p_{sat}(T_{lv})}{RT_{lv}} \quad (A.7)$$

Finally, ∇C_v is defined as:

$$\nabla C_v = \frac{C_v|_{lv} - C_v|_{far}}{L_{far}} \quad (A.8)$$

where $C_v|_{lv}$ is the molar concentration at the interface and $C_v|_{far}$ is the molar concentration at a distance $L_{far} = 3h$, where h is the average structural thickness. The evaporation rate can be calculated by inserting measured temperature values into Eq. A.5.

Appendix : Fluorescence Intensity-Saturation Level Relationship of RhB@PLB

Experimental Method

The fluorescence characteristics of RhB@PLB is analyzed by observing evaporating 0.2 μl RhB@PLB colloidal droplets at room temperature. To characterize the effects of particle size and dye concentration on RhB@PLB's fluorescence intensity, we use sphere diameters ranging from 100 – 1000 nm and dye concentrations ranging from 1% – 6%. The standard experimental set uses 0.1 mM dye concentration, 300 nm spheres, and 4% colloidal concentration. In the course of the experiment, the droplet liquid thickness decreases upon solvent evaporation and alters the top-to-bottom view signals. The issues created by dynamic liquid thickness are addressed by employing inverted confocal microscopes, which maintains a constant focal plane from a bottom-to-top view while being unaffected by liquid thickness changes. In the following droplet experiments, an inverted confocal microscope (LSM 780, ZEISS) with a 10 mm long working distance captures fluorescence signals at 1 s intervals. A filter set (561 nm excitation band pass and 570 – 700 nm emission band pass) with a halogen illumination source is used. The laser intensity, gain, and pinhole are kept consistent throughout all experimental sets.

Characterization of RhB@PLB Droplets.

As the solvent evaporates, the solution can be identified by distinctive saturation regimes based on the solution's fluorescence intensity. Figure A.1a shows fluorescence intensity-based images of a drying RhB@PLB colloidal droplet with respect to time. Immediately after the droplet is dispensed onto the substrate, the RhB@PLB solution is in a saturated regime, where particles drift freely within the solution. As the solution evaporates, the particles are driven towards the droplet peripherals (i.e., growth front) by evaporation-induced water flows generated at the liquid-vapor-

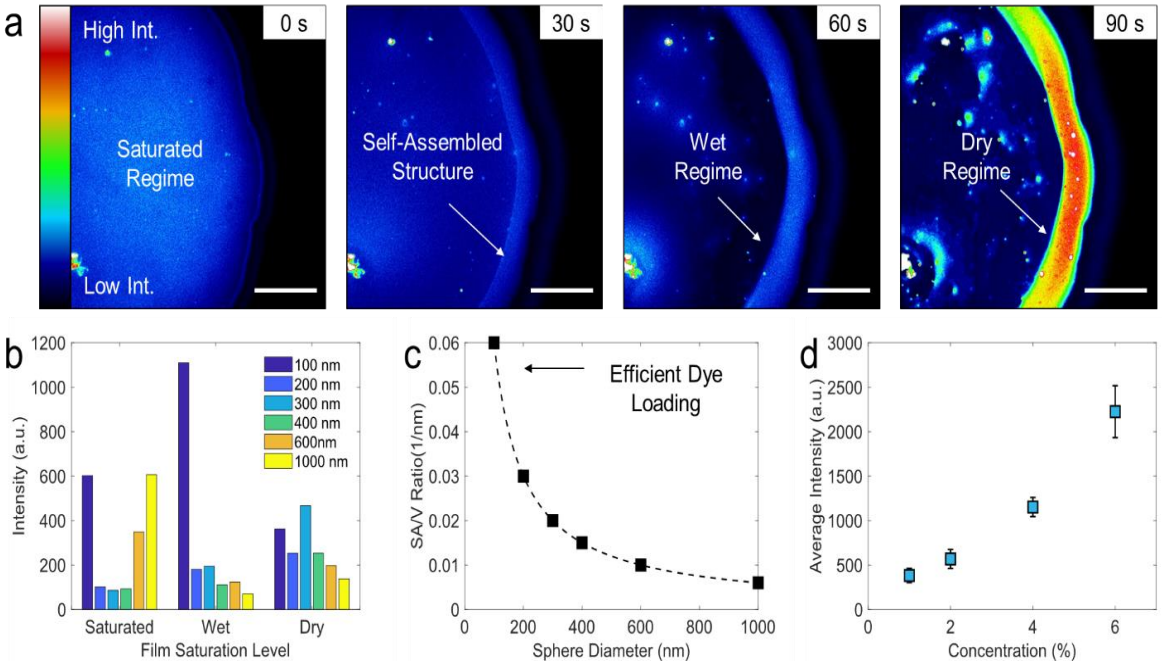

Figure A.1: Saturation level sensitivity of RhB@PLB colloidal droplets. (a) Fluorescence intensity-based images show 300 nm colloidal droplets evaporating with respect to time. The saturated state is defined as the initial fluorescence intensity of the bulk solution at $t = 0$ s. As the solution evaporates, the colloidal nanospheres start assembling into structural organizations at the droplet peripheral ($t = 30$ s). The structural organization is maintained at a wet state until $t = 60$ s by means of capillary wicking. The structure emits an abrupt fluorescence intensity peak upon dry-out ($\sim t = 90$ s). The scale bar is 300 µm. (b) The bar graph displays fluorescence intensity at different saturation levels for varying sphere diameters (100 – 1000 nm). (c) The graph plots surface area to volume ratio (SA/V Ratio) for different sphere diameters. (d) The plot shows average fluorescence intensity of the self-assembled structure after dry-out it. The polystyrene beads are mixed with different dye concentration ratios (1 – 6%). The size of the nanoparticles is 300 nm.

solid interface. The particles at the droplet peripherals aggregate and form packed structures where the microscopic liquid-vapor interfaces between nanoparticles facilitate evaporation even further. The nanopores generated between packed nanoparticles help channel liquid continuously to the

self-assembled structure by means of capillary forces, therefore keeping the structure wet (i.e., wet regime). Upon solution depletion, the fluorescence intensity abruptly increases as the structure dries. The fluorescence intensity peaks upon full dry-out (i.e., dry regime).

We hypothesize that the fluorescence characteristics follow a general fluorescence-saturation level relationship where the fluorescence intensity increases as the overall number of fluorophores per unit volume (i.e., local dye concentration) increases. In detail, the fluorescence intensity increases as the solvent evaporates due to an increase in the local dye concentration as the total number of fluorophores loaded onto nanospheres and the mean distance between doped nanospheres increases and decreases, respectively. The growing number of fluorophores confined in a small space increases their absorption coefficient and results in high fluorescence intensity.[1] In other words, the fluorescence intensity presumably should increase as the system transitions from saturated to dry regimes because the number of fluorophores introduced into the system increases upon evaporation. However, we observe different fluorescence-saturation level relationships when nanoparticle sizes vary. Figure A.1b shows the average fluorescence intensity of saturated, wet, and dry saturation levels of drying colloidal solutions made from different sphere diameters. The nanoparticle size effects on fluorescence-saturation level relationships are explained below.

The fluorescence intensity of the smallest (100 nm) sphere diameter solution increases while it transits from saturated to wet regime but decreases upon dry-out (Figure A.1b). Real-time fluorescence images of the drying 100 nm colloidal droplet provide a full description of the fluorescence decay, showing that the fluorescence intensity continues to increase even after the wet regime develops. However, the fluorescence intensity abruptly decreases by ~67% the moment the liquid completely evaporates (Figure A.1c). The maximum intensity is ~52% higher than the

wet state before fluorescence decay occurs. The continuous increase in fluorescence intensity confirms that the fluorescence intensity increases as saturation level decreases (thus following the general fluorescence-saturation level relationship) but is affected by some factor at the very end of the drying process. We attribute the sudden fluorescence decay to excessive local dye population in confined areas, which can activate non-radiative pathways caused by short-range molecular interactions, also known as aggregation-caused quenching (ACQ).[2, 3] In other words, the restricted interactive spatial domains of smaller sphere sizes cause excessively tight dye-dye interactions that lead to fluorescence decay. It should be noted that solutions with smaller particles emit relatively higher fluorescence intensities because smaller particles have a larger surface area to volume ratios which enables efficient dye loading (Figure A.1c).[4]

For sphere diameters ranging from 200 – 400 nm, the fluorescence intensity excellently follows the general fluorescence-saturation level relationship (Figure A.1c). In this work, we select 300 nm sphere diameters due to its marked fluorescence response to saturation levels. For this sphere size, the colloidal concentration or doped nanosphere population also contributes to fluorescence emission. Figure A.1d shows that dried colloidal structures made from 300 nm diameter spheres emit brighter average fluorescence signals when colloidal concentration is increased. This is because the higher supply of spheres to the growth front creates a thicker medium.[5] At constant 4% colloidal concentration, the fluorescence intensity increases from ~20% – 125% to ~40% – 140% from saturation-to-wet state and wet-to-dry state, respectively (Figure A.1c).

Finally, larger sphere diameters (600 – 1000 nm) exhibit bright-dark-bright transitions for saturated, wet, and dry regimes, respectively. The colloidal solution emits the brightest fluorescence in the saturated regime. The high fluorescence in the saturated regime may be caused by optical

resonances arising from light being trapped by total internal reflections from within a boundary (sphere, disks, and shells) called whispering gallery modes (WGM), also known as morphology dependent resonances (MDR).[6-8] The typical sphere diameters available in WGM related literatures range from 2 – 100 μm.[6-8] We speculate that the relatively large size of the 600 – 1000 nm diameter spheres provide favorable environments for trapping light within the sphere and causing optical resonance. Furthermore, unlike the smaller sphere sizes (100 – 400 nm) the fluorescence intensity decreases when transitioning from saturated to wet states as the spheres form organizations. The fluorescence decrease caused by the excitation light's inability to penetrate through the thick, solid sphere aggregates. Finally, the fluorescence intensity increases ~60% – 90% from wet to dry state, as dye incorporation into the spheres increases upon dry-out.

Temperature Effects on Fluorescence Intensity.

While RhB is widely known for its temperature-sensitivity, the temperature effects in colloidal-dye mixtures are superseded by local dye concentration. For example, plain RhB solutions generally exhibit high fluorescence intensity at low temperatures.[9-11] Since the wet regime in Figure S1a is composed of numerous microscale liquid-vapor interfaces between packed spheres, it has a higher evaporation rate (the high evaporation rate is the source of the water flux that guides particles towards the growth front) than the bulk solution. The high evaporation rate causes the wet regime's temperature to drop and therefore fluoresce brighter. Note that this result is similar to the results arising from local dye concentration effects. However, temperature effects cannot fully explain why fluorescence intensity increases so dramatically (40% – 140%) from wet to dry states. By using conventional fluorescence intensity-to-temperature calibration curves, the temperature differences between the three distinct saturation levels would be overexaggerated and

unrealistic. Therefore, we assume that temperature effects on fluorescence intensity are minimal when compared to the local dye concentration effects on fluorescence intensity in this work.

Fluorescence Reversibility of RhB@PLB.

The RhB@PLB solution exhibits excellent fluorescence reversibility towards the film's saturation level. Real-time measurements of a drying RhB@PLB colloidal droplet show fluorescence intensity peaks upon dry-out (Figure A.2a). Water is re-supplied to the structure via pipetting and the colloidal droplet dries again (Figure A.2b). Both the re-wetted and re-dried states show minimum error of 2% and 12%, respectively. The results suggest a highly reversible relationship between fluorescence intensity and saturation levels.

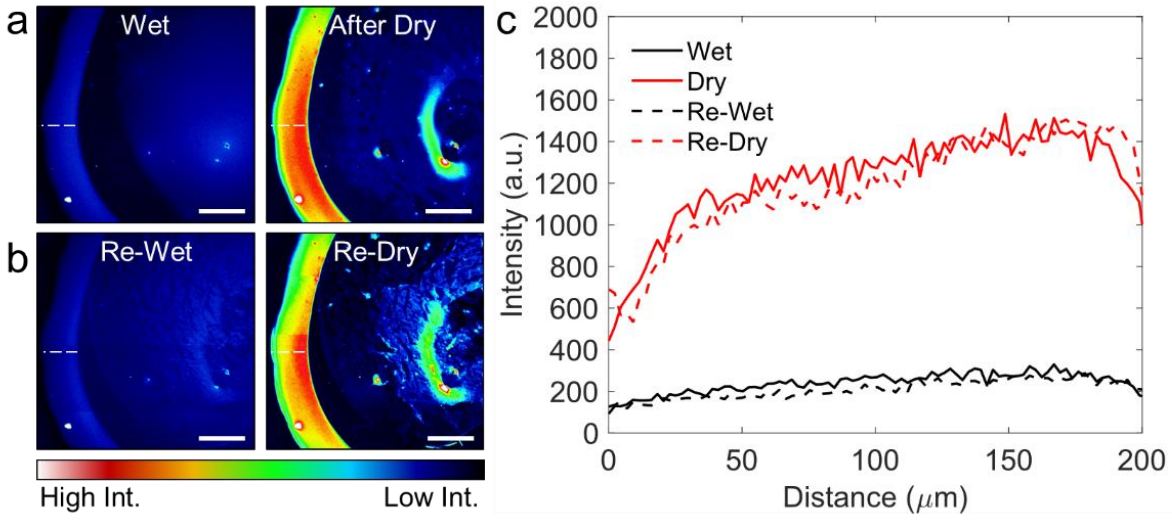

Figure A.2: Reversibility of RhB@PLB colloidal solution. The RhB@PLB colloidal droplets display high reversibility with respect to saturation levels. (a) Fluorescence intensity-based images of 300 nm RhB@PLB colloidal droplets before and after dry-out is shown. (b) The dried colloidal droplet is re-wetted by pipetting water and dried again. The scale bar in (a and b) represents 200 μm. (c) The fluorescence intensity plot of the white dashed line in (a and b) suggests a very high saturation-related fluorescence reversibility of RhB@PLB solutions.

Appendix : Grain Lift-Off

When a pair of both longitudinal and transverse cracks connect, the opal structure becomes an isolated domain (i.e., grain), which is capable of releasing stress by being peeled off from the substrate and bending (i.e., grain lift-off) (Figure A.3). Grain lift-off phenomena is discussed in detail in recent literature, where the surface chemistry of the substrates is tuned to fabricate centimeter-scaled opal stripes via grain lift-off mechanisms.[12] While our cases may not be as extreme, grain lift-off is speculated to be the main cause of the fluorescence intensity discrepancies shown in Figure 3.6c.

To investigate the existence of grain lift-off phenomena and its effect on fluorescence signals, we employ three-dimensional (3D) Z stack imaging to visualize surface height variations. The Z stack imaging of 50 μm depth is performed at 1 μm increments. The top view Z stack fluorescence image in Figure A.3a shows high intensity regions (numbered 1 and 2) where transverse cracks are located. The high intensity regions translate to higher structures. The 3D side view image in Figure A.3b verifies grain lift-off and shows higher structures for the high-intensity regions 1 and 2 in Figure A.3a. We conclude that fluorescence signal discrepancies occur as the lifted local grain areas deviate from the focal plane (Figure A.3c-d). A maximum grain lift-off induced error of 13% is reported in this research.

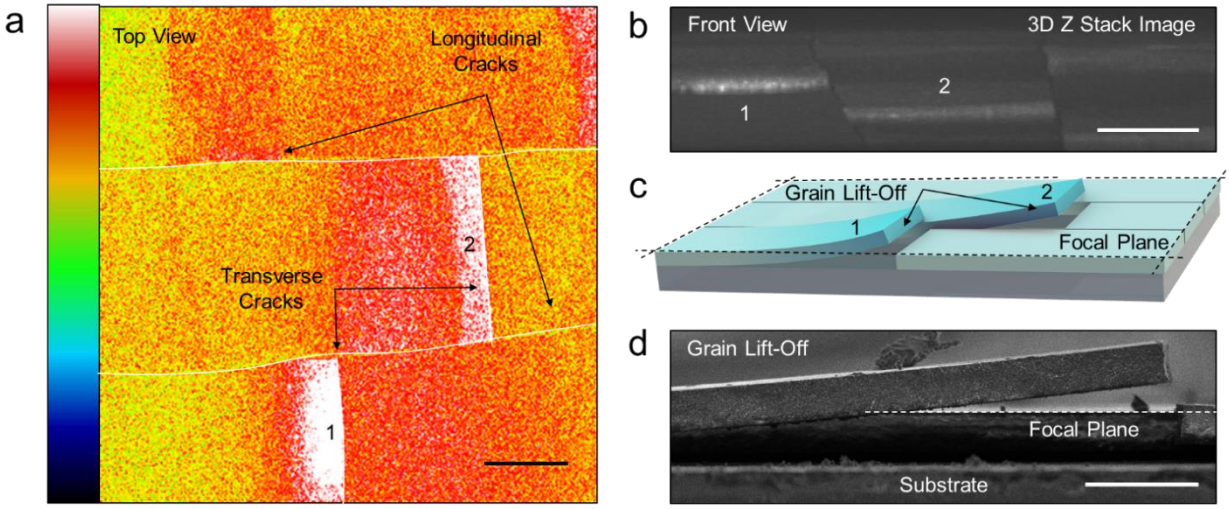

Figure A.3: Grain lift-off effects. (a) The top view fluorescence image of a fully dried film. The scale bar represents 200 μm. (b) A z stack image reconstructs a three-dimensional (3D) image to identify height discrepancies at the film surface. The 3D image exhibits relatively high structures at region 1 and 2. The scalebar is 200 μm. (c) The illustration displays grains lifting off from the glass substrate, causing the structure to move above the focal plane and emit brighter fluorescence signals. (d) Scanning electron microscope (SEM) image confirms grain lift-off phenomena. Scale bar is 50 μm.